Journal of CO2 Utilization 101 (2025) 103204

Contents lists available at ScienceDirect

Journal of CO2 Utilization

journal homepage: www.elsevier.com/locate/jcou

# $CO_2$ utilization and sequestration potential in deep coal seams: A case study on Carboniferous coals from the Karaganda Basin, Kazakhstan

Majid Safaei-Farouji [a,*], David Misch [a], Reinhard F. Sachsenhofer [a], Nikolaos Kostoglou [b], Garri Gaus [c,d], Thorsten Bauersachs [c], Medet Junussov [e], Milovan Fustic [e,f]

[a] Chair of Energy Geosciences, Department of Applied Geosciences and Geophysics, Montanuniversität Leoben, Leoben 8700, Austria
[b] Department of Materials Science, Montanuniversität Leoben, Leoben 8700, Austria
[c] Energy and Mineral Resources Group (EMR), Institute of Organic Biogeochemistry in GeoSystems, RWTH Aachen University, Lochnerstraße 4-20, Aachen 52056, Germany
[d] Fraunhofer Research Institution for Energy Infrastructures and Geotechnologies, Aachen 52062, Germany
[e] School of Mining and Geosciences, Nazarbayev University, Astana, Kazakhstan
[f] Department of Earth, Energy, and Environment, University of Calgary, 2500 University Drive NW, Calgary, AB, T2N 1N4 Canada

ARTICLE INFO

*Keywords:*
CCS
$CO_2$ utilization
$CO_2$-ECBM
Kazakhstan
Karaganda coal basin

ABSTRACT

Kazakhstan is a major coal producer and emitter of carbon dioxide ($CO_2$), presenting both a challenge and an opportunity for $CO_2$ utilization and storage. The main goal of this work is to study the feasibility of $CO_2$ as a feedstock for enhanced coalbed methane recovery ($CO_2$-ECBM), as well as the associated geological storage potential of the D6 coal seam in the Karaganda Basin. For this purpose, coal samples were investigated using elemental analysis, Rock-Eval pyrolysis (RE), organic petrography as well as low-pressure (LP: $N_2$, $CO_2$), and high-pressure (HP: $CO_2$, $CH_4$) sorption tests. Vitrinite reflectance values show that seam D6 reached the medium-volatile bituminous rank. Higher organic matter content significantly increases the LP $CO_2$ sorption capacity. The adsorption-desorption isotherms of $CO_2$ recorded under both LP and HP conditions show a hysteresis loop. This is probably due to interactions between $CO_2$ and functional groups leading to enhanced physisorption at LP and chemisorption and matrix swelling at HP conditions. This effect is favorable for storage purposes as it implies safe $CO_2$ trapping even at reduced reservoir pressure. The CBM potential of seam D6 is estimated at 9 billion $m^3$ initial gas and 360 million $m^3$ producible gas in place. Estimates of the adsorptive and total $CO_2$ storage capacity yielded 1.1 and 3.6 gigatons (Gt), respectively. With this considerable total storage capacity, Kazakhstan's current annual $CO_2$ emissions could be stored for 14 years. This study highlights how $CO_2$ can be effectively utilized as a feedstock to enhance methane recovery while achieving long-term $CO_2$ sequestration.

## 1. Introduction

Kazakhstan is rich in mineral and energy resources including giant coal deposits mainly in Carboniferous and Jurassic horizons. With an annual production of about 112 million tons, the country is the world's 8th largest steam and coking coal producer [60].

Kazakhstan is also a major emitter of $CO_2$ with cumulated $CO_2$ emissions of 255 million tons in 2023 [28]. 78 % of the total $CO_2$ emissions result from fossil fuel combustion at stationary point sources, including electrical power and metallurgical plants [3]. In 2020, Kazakhstan announced its goal to achieve carbon neutrality by 2060 [39]. The complete abandonment of coal use by 2050 is one of the cornerstones of this plan [49].

In parallel to the decarbonization of the energy system and industrial processes, carbon capture and storage (CCS) is an important measure to reduce $CO_2$ emissions. Abuov et al. [3] investigated the $CO_2$ storage potential in depleted oil and gas reservoirs and reported storage potential of 0.2 Gt for depleted oil and 1.0 Gt for depleted gas reservoirs that are readily accessible. In view of the current emission level, however, alternative technologies have to be considered to increase the long-term storage capacity.

An alternative way to store $CO_2$ safely is to inject it into deep coal seams, where the (nano)porous structure of coal offers an extensive storage capacity. Furthermore, the high $CO_2$ adsorption capacity of coal,

* Corresponding author.
*E-mail address:* majid.safaei-farouji@unileoben.ac.at (M. Safaei-Farouji).

https://doi.org/10.1016/j.jcou.2025.103204
Received 20 May 2025; Received in revised form 11 August 2025; Accepted 20 August 2025
Available online 22 August 2025

which even exceeds that of methane, guarantees permanent and safe $CO_2$ storage [17,27,64]. Preferentially, storage options should be developed according to a preceding source-to-sink matching and in the vicinity of emission hot spots. CCS in coal seams could therefore be particularly useful for Kazakhstan, as some of the main $CO_2$ emitters are located in major coal basins. In addition to serving as a long-term storage reservoir, deep coal seams can be used as an active $CO_2$ feedstock sink for methane recovery. Most interesting in this regard is the Karaganda Basin (Fig. 1), which is one of the largest coal-producing regions in Central Asia and hosts significant reserves of Carboniferous bituminous coal. This coal is currently mined in several large underground mines down to a depth of 1200 m [63].

Carboniferous coal seams in the Karaganda Basin are known to be very rich in methane, constituting a major mining risk [59]. The latest methane gas explosion in the Lenin Mine, which is in the focus of the present paper, occurred in 2023 and resulted in around 40 fatalities. On the other hand, the Karaganda Basin holds a significant coalbed methane (CBM) potential, which was estimated from 4.3 to 8.0 trillion $m^3$ [6,19,43,63].

The conventional technique for producing CBM involves reducing the reservoir pore pressure by dewatering, which releases adsorbed and dissolved methane from the matrix and formation water, respectively. The efficiency of this method, however, is typically relatively low (20–60 %; [58]). By leveraging coal's stronger affinity for $CO_2$ compared to $CH_4$, CBM production can be enhanced through $CO_2$ injection. This technique, known as $CO_2$-enhanced coalbed methane ($CO_2$-ECBM; [82,85,72]), combines CBM production with $CO_2$ sequestration. This dual-purpose approach not only enhances CBM extraction but also reduces the costs associated with $CO_2$ storage operations [20].

The primary goal of the present work is to investigate the $CO_2$ storage capacity of Carboniferous coal in the Karaganda Basin, using the D6 seam of the Lenin Mine – the most significant coal seam in the western part of the basin (Sherubay-Nura Trough; Fig. 1) – as an example. This seam contains up to 36 $m^3$ /t $CH_4$ [6], and therefore, CBM potential of the D6 seam is also evaluated from a resource perspective. The aims of this study are aligned with the broader goal of minimizing greenhouse gas emissions in Kazakhstan, while providing access to natural gas resources, which could bridge the energy gap caused by a phase-out of coal production.

## 2. Geological setting

The Karaganda Basin is located north of the Hercynian Jungar-Balkash foldbelt [70]. It overlies pre-Carboniferous rocks of the Kazakhstan Plate. With a West-East extension of ~120 km and North-South (N-S) extension of 30–50 km, the Karaganda Basin covers

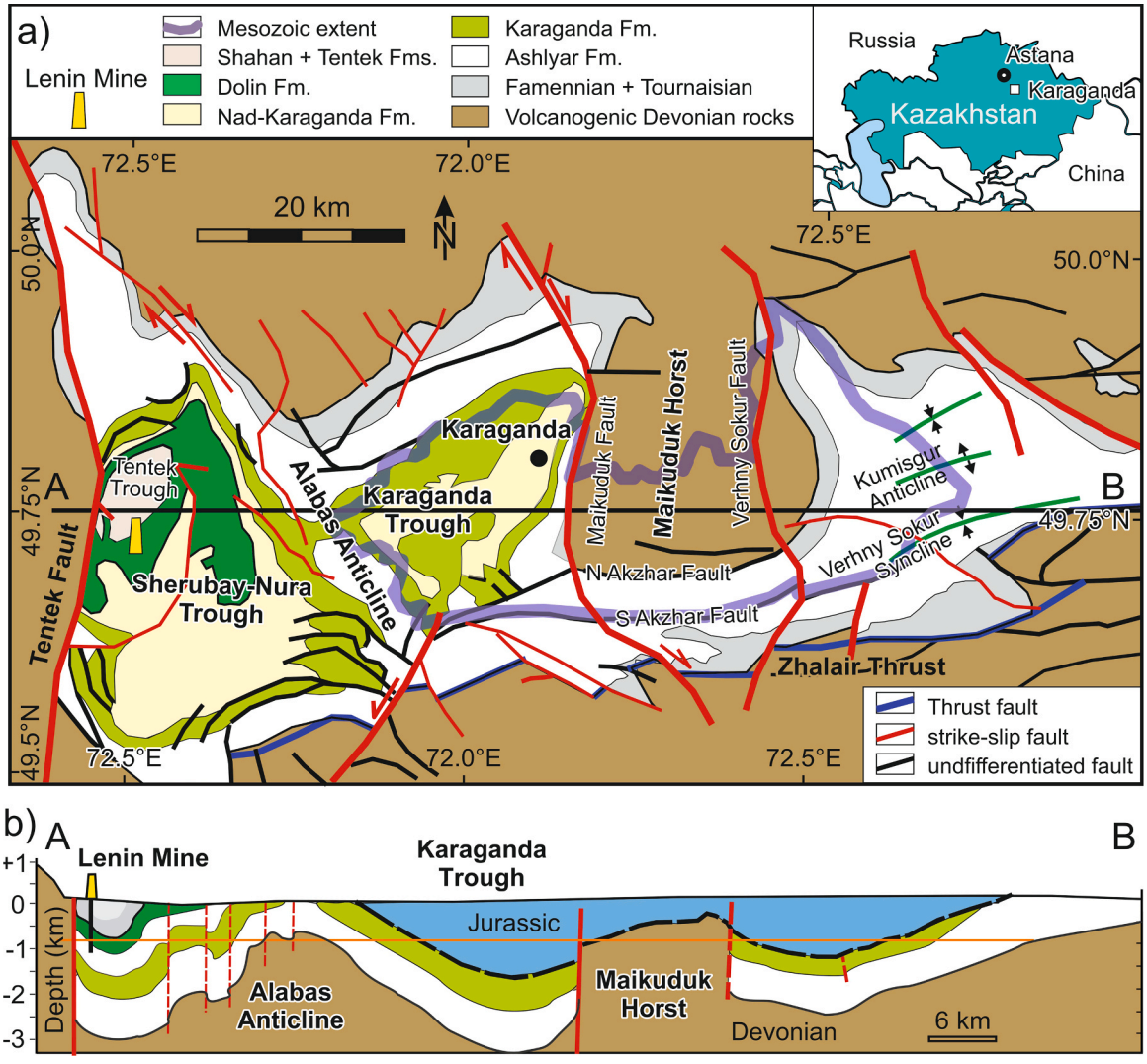


**Fig. 1.** a) Geological map of the coal-bearing Karaganda Basin. b) West-East cross-section; the horizontal orange line in b) indicates the depth cut-off for currently unmineable coal seams and supercritical conditions for $CO_2$ (modified after [1]).

an area of ~3600 km², of which about 2000 km² are coal-bearing (Fig. 1; [22]). The total thickness of the Carboniferous and younger sediments in the Karaganda Basin reaches 5 km [1].

The Karaganda Basin is bordered to the south by the Zhalair Thrust (Fig. 1a), along which Devonian rocks overthrusted the Carboniferous deposits during Late Carboniferous to Permian (Hercynian) time [1]. The western border is formed by the N-S trending Tentek Fault, which is a major strike-slip fault of unknown, but probably Permo-Triassic age with a displacement in the order of 4–5 km ([47]; Fig. 1a). Devonian sedimentary and volcanic rocks are exposed along the northern basin margin. The Alabas Anticline and the Maikuduk Horst subdivide the Karaganda Basin into three troughs. These are, from west to east, the Sherubay-Nura Trough (including the Tentek Trough), the Karaganda Trough, and the Verhny Sokur Trough (Fig. 1).

The sedimentary succession in the Karaganda Basin (Fig. 2) accumulated in a foreland basin setting and starts with Upper Devonian (Famennian) and lowermost Carboniferous (Tournaisian) marls and limestones [63]. Interbedded sandstone, mudstone, and coal layers, along with volcanic ash layers, dominate in the Visean to Upper Carboniferous succession, which is subdivided into seven formations [1]. The Lower Carboniferous (Mississippian) Ashlyar and Karaganda and the Upper Carboniferous (Pennsylvanian) Dolin and Tentek formations contain commercial coal seams (Fig. 2). Overall, 60 coal seams with a total thickness of 70–105 m are considered economic [1]. The most important seams are found in the Karaganda and Dolin formations.

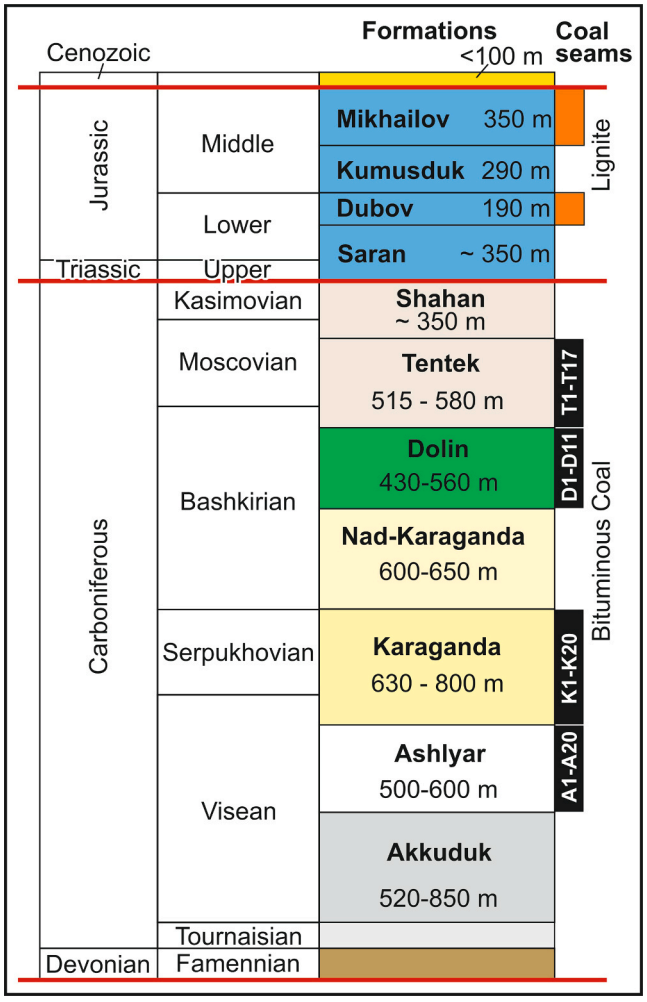


**Fig. 2.** Simplified stratigraphic column of the basin fill in the Karaganda Basin (after [1,63]). The distribution of Carboniferous coal seams is shown together with seam codes. Jurassic coal seams are lignites. Red lines indicate major unconformities.

The Karaganda Formation includes up to 40 coal seams; the main seams are labelled from base to top K1 to K20. Some of the seams are up to 4.5 m thick (exceptionally 12 m). The Dolin Formation also contains up to 40 seams, but only 11 of the seams have labels (D1–11). The thickness of the laterally very continuous D6 seam is 4.7–6.3 m, while other D seams are only 1.0–1.5 m thick [1].

The D6 seam, which is in the focus of the present work, is currently exploited in four mines (Lenin, Kazakhstan, Tentek, Shakhtinsk) in the western part of the Karaganda Basin. It contains high-quality coking coal interbedded with few cm- to dm-thick partings [7]. The coal is methane-rich and prone to outbursts, especially in its bottom part, which is characterized by a distinct 0.2–1.2-m-thick shear zone with friable coal [6]. The methane content of the D6 seam increases with depths from 3–18 $m^3$/t at a depth of 180–250 m to 18–28 $m^3$/t (301–600 m), 30–32 $m^3$/t (601–900 m), and even 23–36 $m^3$/t (900–1500 m) [6].

Major uplift and erosion occurred after the Carboniferous and before the deposition of Upper Triassic (Rhaetian) and Jurassic rocks. In the eastern Verhny Sokur Syncline and the central Karaganda Trough, erosion removed large parts of the Upper Carboniferous succession, while the complete Carboniferous section is preserved in the western Sherubay-Nura Trough (Fig. 1b).

The Mesozoic succession is preserved in the Karaganda Trough and the western part of the Verhny Soku Syncline (Fig. 1b) and can attain a thickness of more than 1000 m (Fig. 2). The non-marine succession starts with locally very thick basal conglomerates (Saran Formation) and grades into sandstones, clays, and sands. Lignite seams are present in the Lower Jurassic Dubov and the Middle Jurassic Mikhaylov formations. The lignite in the Mikhaylov Formation was up to 28 m thick but was completely mined out. The Cenozoic and Quaternary cover of the Karaganda Basin is thin [1,63].

## 3. Materials and methods

### 3.1. Samples

Seventeen samples were collected from the D6 seam in the Lenin Mine in the western part of the Karaganda Basin (Tentek mining district in the Sherubay-Nura Trough). Access conditions necessitated sampling of the 5.3 m thick seam at two nearby sites, both situated approximately 750 m below the surface. A single sample from the underlying coaly shale (D6L1) and five coal samples from the lower part of the seam (D6L2–6) were collected in "Koverny 403D62w", while the eleven samples from the upper part of the seam (from bottom to top: D6U10–0) were collected in longwall "405D61w". Sample D6L2 represents the soft, gas-rich shear zone at the base of the seam. All samples are point samples and represent about 10 cm of the seam.

Bulk geochemical and petrographic parameters were determined for all samples. Five representative samples were selected for subsequent gas adsorption analyses. This sub-set includes the gas-rich sample from the basal part of the seam and four samples distributed evenly across the seam.

### 3.2. Bulk parameters and organic petrography

The total organic carbon (TOC) and total sulfur (S) contents in the coals were measured using an Eltra Helios C/S analyzer. Rock-Eval 6 pyrolysis provided measurements of free hydrocarbons ($S_1$ peak), hydrocarbons produced during pyrolysis ($S_2$ peak), and temperature at peak hydrocarbon generation ($T_{max}$). $S_1$ and $S_2$ were used to calculate the bitumen index (100 ×$S_1$/TOC), the quality index (100 ×[$S_1$+$S_2$]/TOC; [73]), and the hydrogen index (100 ×$S_2$/TOC) [23]. The ash yield was determined following ASTM D1374 [4].

For organic petrography, samples were crushed to a maximum size of 1 mm and embedded in epoxy resin [40]. The polished blocks were

investigated with a Leica incident light microscope equipped with a 50 × oil immersion objective. Maceral investigation involved counting 500 points using white incident and blue light excitation, and a single-scan approach [41,74]. The maceral terminology followed the International Committee for Coal and Organic Petrology (ICCP) system [37,38]. Vitrinite reflectance (%Rr) was measured using non-polarized light at a wavelength of 546 nm with a magnification of 50 ×, employing the Hilgers Fossil software. For each sample, 100 measurement points were taken to calculate the mean vitrinite reflectance and standard deviation [42].

### 3.3. Low-pressure $N_2$ and $CO_2$ adsorption

The selected five samples were crushed and sieved to achieve a particle size of 0.18–0.25 mm (60–80 mesh). Subsequently, the powdered samples were dried at 40 °C for 12 h in a vacuum oven to eliminate moisture. A manometric Autosorb iQ$^3$ gas sorption analyzer (Anton-Paar QuantaTec, USA) was employed for the adsorption analyses of $N_2$ (99.999 % purity) and $CO_2$ (99.995 % purity).

Prior to the gas adsorption measurements, approximately 1 g of each sample was degassed at 105 °C for 24 h under vacuum in the Autosorb iQ$^3$ degassing station to remove any residual moisture and pre-adsorbed gases, while preserving the chemical composition of the coals.

The adsorption and desorption isotherms of $N_2$ were recorded at a relative pressure range ($P/P_0$) of 0.01–0.995, where P represents the equilibrium gas pressure in the system and $P_0$ denotes the saturation pressure of the adsorbate. In contrast, the isotherms for $CO_2$ were recorded within an absolute pressure range of 0.00012–0.106 MPa (120–106000 Pa).

Temperature conditions varied depending on the gas type: $N_2$ measurements were conducted at 77 K using a liquid $N_2$ bath for temperature control. $CO_2$ measurements were performed at 273 K, utilizing a recirculating bath containing a mixture of distilled water and antifreezing liquid.

The specific surface area (SSA) values were determined based on the Brunauer-Emmett-Teller (BET) model, whereas the Barrett-Joyner-Halenda (BJH) model was applied to $N_2$ adsorption isotherms to determine specific pore volume (SPV) and pore size distribution (PSD). For the BJH analysis, the adsorption branch was chosen over the desorption branch to avoid false peaks (artifacts) that can occur due to cavitation-induced evaporation phenomena [45]. Detailed information regarding the BET and BJH methods is available in Li et al. [53]. It should be noted that the present study follows the nanopore size classification standards of the International Union of Pure and Applied Chemistry (IUPAC) [75].

### 3.4. High-pressure $CO_2$ and $CH_4$ adsorption

High-pressure gas expansion tests (up to 20 MPa and 318 K) with the reference gas He, $CO_2$ and $CH_4$ were conducted using a calibrated manometric setup (Fig. 3). This setup comprised a stainless-steel sample cell, two high-pressure shutoff valves, and a high-precision pressure transducer (Keller AG, Series 33X) connected by 1/16″ stainless steel capillaries inside a temperature-controlled oven. Additionally, a gas supply system was installed upstream of the oven, allowing He, $CH_4$ or $CO_2$ to be injected directly from gas cylinders or stored in a piston pump (Teledyne Isco) and pressurized prior to injection.

Samples were dried in a vacuum oven at 105 ℃ until constant weight was achieved (< 0.005 g weight change in 24 h) and then placed in the high-pressure sample cell. The system was evacuated for at least 24 h prior to measurement and temperature was set to 318 K. Helium (He) was introduced into the reference cell, and after equilibrium was reached, the gas was expanded into the sample cell. Gas uptake was monitored until pressure equilibration (< 500 Pa h$^{-1}$). He, as a non-adsorbing reference gas, provided an estimate of the sample's free gas storage capacity [kg gas t$^{-1}$ rock] and skeletal density [$\rho_{sk}$ in g cm$^{-3}$ ]. At least three He cycles were performed to assess reproducibility. Following He measurements, the system was evacuated again for at least 24 h. $CH_4$ or $CO_2$ was then introduced using the piston pump to control the injection pressure. The reference cell was filled to the desired pressure, equilibrated, and then expanded into the sample cell. Gas uptake again was monitored until pressure equilibration (< 500 Pa h$^{-1}$), representing a combination of volumetric and adsorptive storage capacity [kg gas t$^{-1}$ rock]. Pressure was then increased stepwise to construct an isotherm, typically ranging from approximately 0.2 MPa to 20 MPa, with at least 10 measurement points per isotherm. Additionally, a GeoPyc device (Micromeritics) was used for bulk density determination of coal fragments. Skeletal and bulk densities were used to deduce porosity and specific pore volume:

$$\theta = 1 - \frac{\rho_b}{\rho_{sk}} \quad \text{(Eq. 1)}$$

$$V_{sp} = \frac{1}{\rho_b} - \frac{1}{\rho_{sk}} \quad \text{(Eq. 2)}$$

With: $\theta$ = porosity [unitless] $\rho_b$ = bulk density [g cm$^{-3}$] $\rho_{sk}$ = skeletal density [g cm$^{-3}$] $V_{sp}$ = specific pore volume [m$^3$ kg$^{-1}$]

$CH_4$ and $CO_2$ excess sorption capacities were then determined by using the following mass balance equations:

$$m_{excess} = m_{trans} - \rho_{CH_4/CO_2}(P_{eq}, T) \times V_{Void} \quad \text{(Eq. 3)}$$

$$m_{trans} = \left(\rho_{CH_4/CO_2}(P_{rc}, T) - \rho_{CH_4/CO_2}(P_{eq}, T)\right) \times V_{rc} \quad \text{(Eq. 4)}$$

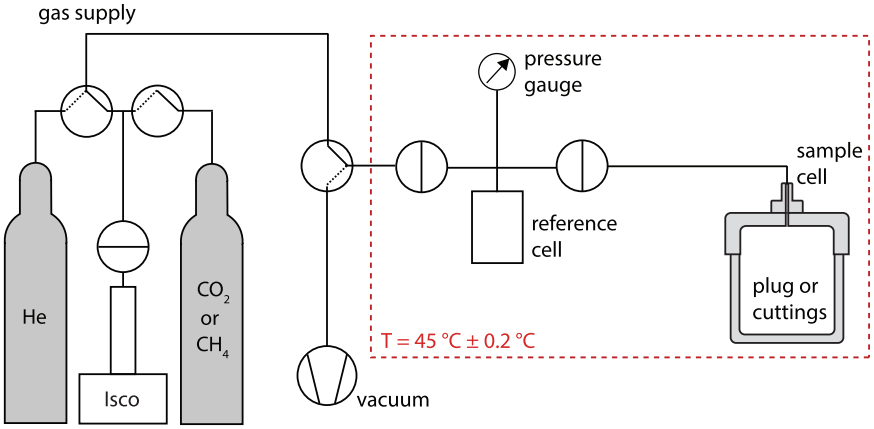


**Fig. 3.** Schematic of the manometric gas expansion setup and upstream gas supply system.

With:$m_{excess}$ = excess sorption$m_{trans}$ [kg] = the difference between the cumulative mass of $CH_4/CO_2$ transferred from reference cell volume to void volume and the mass of free $CH_4/CO_2$ occupying void volume at the respective equilibrium pressures and temperatures$V_{rc}$ = reference cell volume [$m^3$ ]$V_{Void}$ = void volume [$m^3$ ]$P_{rc}$ [Pa] = equilibrated pressures in the reference cell volume prior to expansion into the sample cell volume at given temperature [T in K]$P_{eq}$ [Pa] = equilibrated pressure in the total system volume after expansion into the sample cell at a given temperature [T in K]$\rho_{CH_4/CO_2}$ [kg $m^{-3}$] = $CH_4$ and $CO_2$ densities (calculated using the GERG equation of state [48].

Excess sorption capacity [$n_{excess}$ in mol $kg^{-1}$] was then calculated by:

$$n_{excess}(P_{eq}, T) = \frac{m_{excess}}{M} \frac{(P_{eq}, T)}{m} \quad \text{(Eq. 5)}$$

With:M = molar mass of the respective gas [kg $mol^{-1}$]m = sample mass [kg].

Excess sorption was parametrized using:

$$n_{excess} = n_L \frac{P}{P_L + P} \times \left(1 - \frac{\rho_{CH_4/CO_2}}{\rho_{adsorbed}}\right) \quad \text{(Eq. 6)}$$

With:$n_{excess}$ [mol $kg^{-1}$] = excess amount of $CH_4/CO_2$ adsorbed at specific equilibrium pressures (P [Pa]) and temperatures (T [K])$P_L$ [Pa] = Langmuir pressure, which is the pressure at which half of the adsorption sites are occupied$n_L$ [mol $kg^{-1}$] = maximum Langmuir capacity, or the amount of $CH_4/CO_2$ adsorbed when all sites are occupied$\rho_{CH4/CO2}$ [kg $m^{-3}$] = $CH_4/CO_2$ density at the given equilibrium P and T$\rho_{adsorbed}$ [kg $m^{-3}$] = density of the adsorbed phase that was fixed at 422.6 and 1101 kg $m^{-3}$ for $CH_4$ and $CO_2$, respectively (liquid densities of $CH_4$ and $CO_2$)

Parametrization was achieved by a least square fitting of experimental data by adjusting of $n_L$ and $P_L$. A detailed explanation on sorption capacity mechanisms and parameterization is given in Weniger et al. [81] and Gasparik [26].

### 3.5. CCS and $CO_2$-ECBM estimations

To estimate the $CO_2$-ECBM and resulting CCS potentials of the D6 seam, first the initial $CH_4$ in place (IGIP; Eq. 7) and the producible $CH_4$ in place (PGIP; standard conditions [$cm^3$]; Eq. 8) [76,81] have been calculated following the equations below:

$$\text{IGIP} = A \times TH \times \rho_{coal} \times GC \quad \text{(Eq. 7)}$$

With:A= areal extent of the coal seam ($m^2$)TH = cumulative coal thickness (m)$\rho_{coal}$= coal skeletal density (t/$m^3$)GC= CBM content in the seam ($m^3$/t)

It should be noted that IGIP represents the total volumetric estimate of methane initially stored within the coal seam before any production and recovery. IGIP therefore represents an estimate of maximum $CH_4$ in place and does not account for practical $CH_4$ extraction efficiency.

$$\text{PGIP} = \text{RF} \times \text{CF} \times \text{IGIP} \quad \text{(Eq. 8)}$$

With:RF = recovery factor (proportion of gas fraction that can be extracted by reducing reservoir pressure via water production)CF = completion factor (fraction of area that can be accessed through drilling operations; [81]).

The producible gas in place (PGIP) here estimates the fraction of initial $CH_4$ in place that can be produced considering common efficiency factors.

Considering the prime target to store $CO_2$ during gas production, RF also denotes the storage efficiency of $CO_2$ and typically varies from 0.2 to 0.6 (mainly 0.4; [34,76,81]). Conservative estimates assume that only 10 % of the area of a coal seam may be suitable for $CO_2$ storage, resulting in a CF of 0.1 (e.g., [34,81]).

Hendriks et al. [34] estimated the global $CO_2$ storage potential in different types of underground reservoirs. For coal basins under $CO_2$-ECBM operations, the $CO_2$ storage capacity ($S_{CO2}$) was calculated using the following equation:

$$S_{CO_2} = PGIP \times ER \times \rho_{CO_2} \quad \text{(Eq. 9)}$$

With:ER = exchange ratio between $CO_2$ and $CH_4\rho_{CO_2}$ = $CO_2$ density at standard temperature and pressure (1.977 kg/$m^3$)

## 4. Results

### 4.1. Bulk parameters

Bulk geochemical and compositional parameters are presented in Table 1 and Fig. 4. As expected, the carbonaceous (coaly) shale underlying the seam (D6L1) has relatively low TOC (6.32 wt%) and sulfur contents (0.13 wt%) but shows a very high ash yield (86.9 wt%). The ash yield of the studied coal samples varies strongly from 4.4 to 33.0 wt % (average 11.0 wt%). This variation is reflected by strongly varying TOC contents (56.5–86.6 wt%; average 80.4 wt%). High ash yields and low TOC contents are mainly found in the lower part of the seam including its basal part. Sulfur contents are generally low and range from 0.28 to 0.59 wt% (average 0.44 wt%). The coal is largely free of carbonate minerals.

The amount of $S_1$ and $S_2$ hydrocarbons is lower in the underlying coaly shale than in the coal samples. In the coal samples, $S_1$ and $S_2$ increase with increasing TOC content. The hydrogen index (HI) is low (76 mg HC/g TOC) in the coaly shale, varies between 130 and 189 mg HC/g TOC (avg. 156 mg HC/g TOC) in the lower part of the seam and is very uniform in its upper part (147–179 mg HC/g TOC) (Table 1; Fig. 4). The $T_{max}$ ranges from 463 to 470 °C (average 466 °C).

### 4.2. Organic petrography

Vitrinite reflectance values are uniform (1.15–1.24 %Rr; average 1.22 %Rr; Table 2) and in general agreement with the $T_{max}$ range determined by Rock Eval pyrolysis. Due to the advanced maturity, no primary liptinite macerals are present. Vitrinite group macerals are more abundant (70–99 vol%) than inertinite macerals (1–33 vol%; Table 2; Fig. 4). Relatively high inertinite contents occur in samples D6L4 and D6L5 from the lower part of the seam and in the uppermost 1 m of the seam (Table 2; Fig. 4). Collotelinite is the predominant vitrinite maceral, while degradofusinite and inertodetrinite are the most abundant inertinite macerals (Table 2). The lower part exhibits a high concentration of detrital macerals, such as collodetrinite, vitrodetrinite, and inertodetrinite. Collodetrinite is absent in the upper section, while fusinite contents are relatively high in the uppermost samples (Table 2).

### 4.3. Low-pressure $N_2$ adsorption

Fig. 5 shows the $N_2$ adsorption-desorption isotherms obtained at 77 K for the five samples selected from both the upper and lower sections of the D6 seam. The adsorption-desorption behavior of all samples is similar, with a distinctive hysteresis loop forming at $P/P_0$ values greater than approximately 0.5. Furthermore, none of the samples' adsorption branch reaches a distinct saturation point at $P/P_0$ ~0.99; instead, it increases in a vertical trend.

The BET-SSA and BJH-SPV of the samples range from 1.33 to 7.55 $m^2$/g and 0.004–0.028 $cm^3$/g, respectively. The mean equivalent mesopore diameter of the samples varies from 7.13 nm to 9.76 nm. It is worth noting that pore diameter estimations are unreliable for poorly-defined geologic samples with low mesoporosity. Sample D6L2 stands out with notably higher values across all adsorption parameters and shows the highest BET-SSA (7.55 $m^2$/g), BJH-SPV (0.028 $cm^3$/g), mean equivalent pore size (9.76 nm), and maximum adsorbed $N_2$ volume (18.94 $cm^3$/g @STP) (Table 3; Fig. 5).

**Table 1**
Ash yield, calcite percentage, TOC, sulfur content, and Rock-Eval parameters of the investigated samples from the D6 seam. Grey shading indicates samples selected for adsorption measurements.

| Sample | Position | Ash | Calcite | TOC | Sulfur | $S_1$ | $S_2$ | HI | $T_{max}$ |
|---|---|---|---|---|---|---|---|---|---|
| | (m below top) | (wt%) | | | | (mg HC/g rock) | | (mg HC/g TOC) | (°C) |
| D6U0 | 0.10 | 7.9 | 0.00 | 83.65 | 0.48 | 10.54 | 132.8 | 159 | 467 |
| D6U1 | 0.35 | 15.1 | 0.00 | 77.31 | 0.43 | 11.34 | 113.4 | 147 | 466 |
| D6U2 | 0.60 | 7.7 | 0.00 | 83.93 | 0.44 | 12.36 | 142.2 | 169 | 464 |
| D6U3 | 0.85 | 9.5 | 0.00 | 82.55 | 0.44 | 12.22 | 123.1 | 149 | 466 |
| D6U4 | 1.10 | 7.2 | 4.26 | 83.96 | 0.46 | 13.35 | 147.6 | 176 | 466 |
| D6U5 | 1.35 | 9.1 | 3.69 | 82.71 | 0.45 | 12.95 | 147.9 | 179 | 465 |
| D6U6 | 1.60 | 5.4 | 0.00 | 86.61 | 0.44 | 12.80 | 146.0 | 169 | 463 |
| D6U7 | 1.85 | 7.6 | 0.00 | 84.08 | 0.43 | 13.11 | 147.5 | 175 | 470 |
| D6U8 | 2.10 | 10.9 | 0.00 | 80.53 | 0.41 | 12.42 | 136.1 | 169 | 466 |
| D6U9 | 2.35 | 5.5 | 0.00 | 86.38 | 0.43 | 12.04 | 139.9 | 162 | 463 |
| D6U10 | 2.60 | 8.2 | 8.95 | 83.07 | 0.44 | 12.55 | 137.8 | 166 | 467 |
| D6L6 | 2.80 | 4.9 | 0.00 | 86.59 | 0.46 | 12.42 | 164.1 | 189 | 463 |
| D6L5 | 3.20 | 33.0 | 0.55 | 57.55 | 0.28 | 7.51 | 74.8 | 130 | 466 |
| D6L4 | 4.00 | 7.3 | 0.00 | 84.40 | 0.43 | 11.92 | 131.9 | 156 | 466 |
| D6L3 | 4.55 | 4.4 | 0.00 | 86.52 | 0.50 | 11.33 | 144.6 | 167 | 465 |
| D6L2 | 5.25 | 31.7 | 0.00 | 56.47 | 0.59 | 7.73 | 77.6 | 137 | 468 |
| D6L1 | 5.40 | 86.9 | 2.73 | 6.32 | 0.13 | 0.66 | 4.8 | 76 | 470 |

TOC: total organic carbon; $S_1$: free hydrocarbons; $S_2$: hydrocarbons produced during pyrolysis; and $T_{max}$: temperature at peak hydrocarbon generation ($T_{max}$).

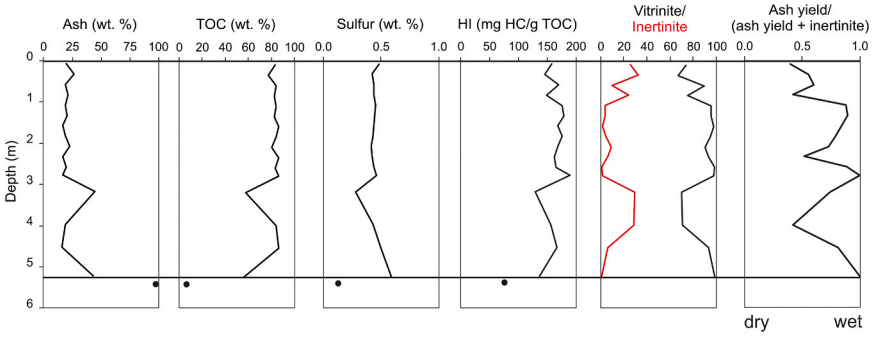


**Fig. 4.** Vertical distribution of ash yield, TOC, sulfur content, hydrogen index (HI), maceral proportions, and ash-inertinite ratio in the D6 seam. The black dots highlight the carbonaceous shale sample. The ash-inertinite ratio indicates cyclic variations between wet and dry periods. Note: the vertical axis shows depth below top of the seam. Maceral percentages are given in vol%.

**Table 2**
Vitrinite reflectance (%Rr) and maceral percentages (vol%) for the studied coal samples.

| Sample | Vitrinite reflectance (% Rr) | Telinite | Collotelinite | Collodetrinite | Vitrodetrinite | Macrinite | Inertodetrinite | Fusinite | Semifusinite | Sum vitrinite | Sum inertinite |
|---|---|---|---|---|---|---|---|---|---|---|---|
| D6U0 | 1.22 | 16 | 58 | 0 | 0 | 1 | 7 | 12 | 6 | 74 | 26 |
| D6U1 | 1.16 | 12 | 51 | 0 | 4 | 1 | 9 | 12 | 11 | 67 | 33 |
| D6U2 | 1.23 | 3 | 86 | 0 | 1 | 0 | 4 | 5 | 1 | 90 | 10 |
| D6U3 | 1.25 | 5 | 70 | 0 | 1 | 0 | 7 | 13 | 4 | 76 | 24 |
| D6U4 | 1.15 | 5 | 90 | 0 | 1 | 0 | 2 | 1 | 1 | 96 | 4 |
| D6U5 | 1.20 | 6 | 90 | 0 | 0 | 0 | 2 | 1 | 1 | 96 | 4 |
| D6U6 | 1.19 | 1 | 97 | 0 | 0 | 0 | 1 | 1 | 0 | 98 | 2 |
| D6U7 | 1.24 | 2 | 93 | 0 | 0 | 0 | 2 | 2 | 1 | 95 | 5 |
| D6U8 | 1.24 | 2 | 89 | 0 | 0 | 1 | 3 | 4 | 1 | 91 | 9 |
| D6U9 | 1.18 | 4 | 90 | 0 | 0 | 0 | 1 | 5 | 0 | 94 | 6 |
| D6U10 | 1.23 | 9 | 90 | 0 | 0 | 0 | 0 | 1 | 0 | 99 | 1 |
| D6L6 | 1.21 | 34 | 56 | 8 | 0 | 0 | 2 | 0 | 0 | 98 | 2 |
| D6L5 | 1.23 | 0 | 58 | 1 | 11 | 0 | 14 | 11 | 5 | 70 | 30 |
| D6L4 | 1.19 | 0 | 36 | 35 | 0 | 0 | 11 | 10 | 8 | 71 | 29 |
| D6L3 | 1.26 | 7 | 85 | 0 | 2 | 0 | 3 | 1 | 2 | 94 | 6 |
| D6L2 | 1.17 | 5 | 64 | 0 | 30 | 0 | 1 | 0 | 0 | 99 | 1 |

### 4.4. *Low-pressure $CO_2$ adsorption*

Fig. 6 displays the $CO_2$ adsorption isotherms recorded at 273 K and up to ~0.1 MPa for the coal samples. All samples exhibit comparable adsorption behavior, with $CO_2$ uptake rising as pressure increases. Sample D6L2 shows the lowest $CO_2$ uptake, which contradicts its high $N_2$ adsorption capacity (see Table 3).

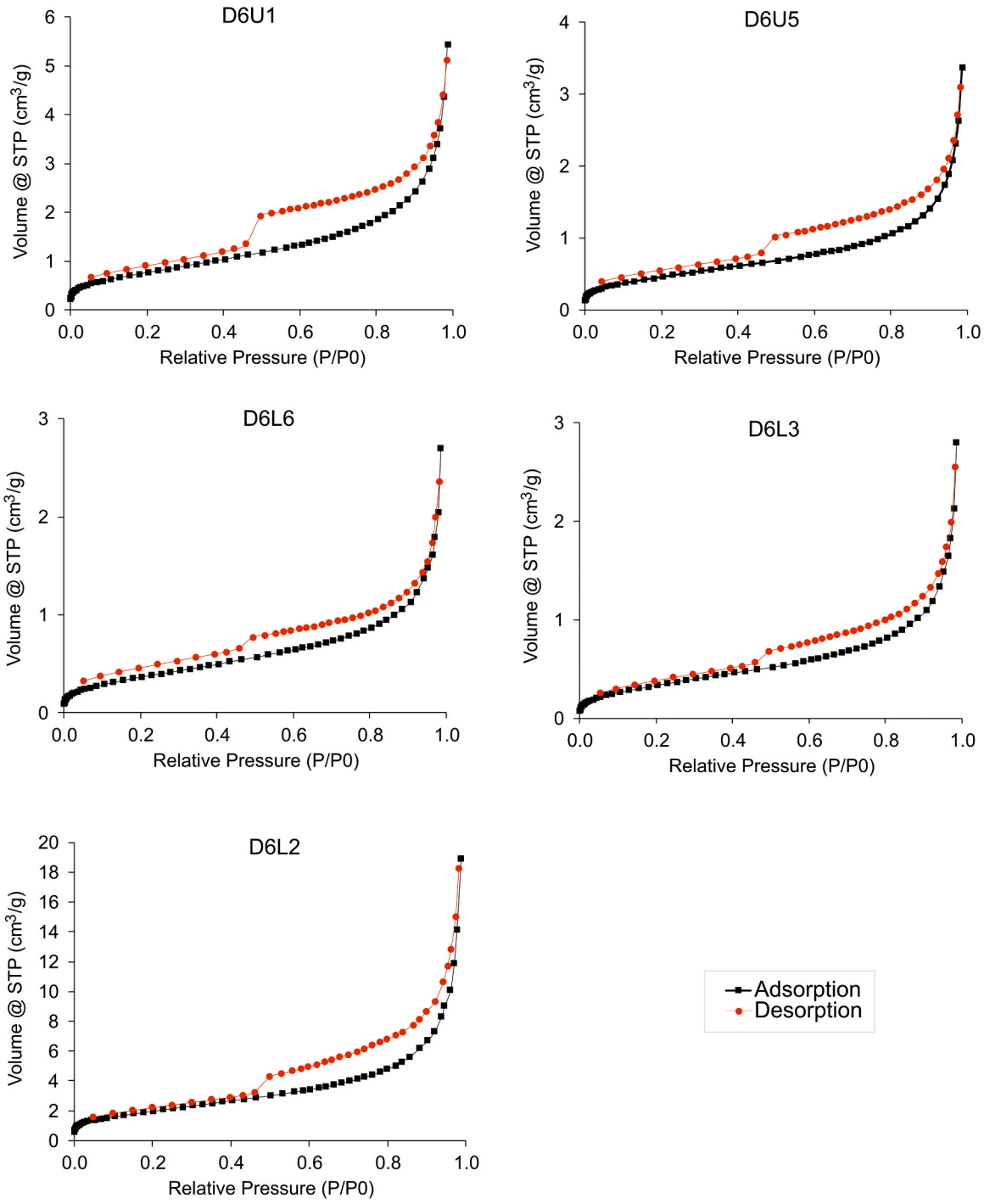


**Fig. 5.** $N_2$ adsorption and desorption isotherms of the coal samples recorded at 77 K.

**Table 3**
Parameters obtained by LP $N_2$ (77 K) and $CO_2$ (273 K) adsorption measurements.

| Sample | BET-SSA ($m^2$/g) | BJH SPV ($cm^3$/g) | Equivalent pore diameter (nm) | Maximum adsorbed $N_2$ volume ($cm^3$/g @STP) | Maximum adsorbed $CO_2$ volume ($cm^3$/g @STP) | Maximum $CO_2$ uptake (mmol/g) |
|---|---|---|---|---|---|---|
| D6U1 | 2.88 | 0.008 | 7.99 | 5.44 | 11.01 | 0.49 |
| D6U5 | 1.73 | 0.005 | 7.41 | 3.37 | 11.90 | 0.53 |
| D6L6 | 1.40 | 0.004 | 7.13 | 2.70 | 12.30 | 0.55 |
| D6L3 | 1.33 | 0.004 | 7.66 | 2.80 | 12.48 | 0.56 |
| D6L2 | 7.55 | 0.028 | 9.76 | 18.94 | 9.64 | 0.43 |

BET-SSA: BET-specific surface area; BJH-SPV: Barrett-Joyner-Halenda-specific pore volume.

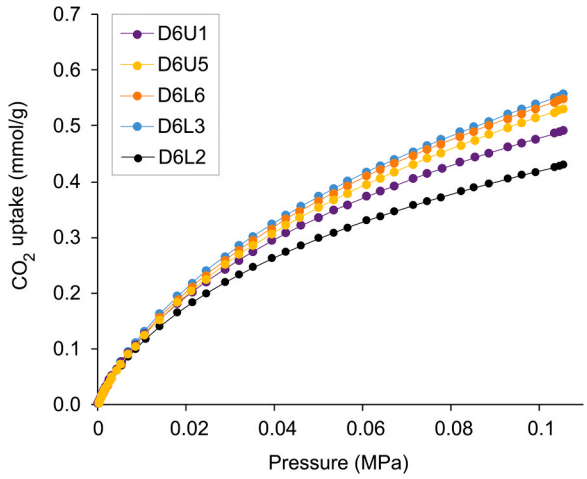


**Fig. 6.** $CO_2$ adsorption isotherms of the coal samples recorded at 273 K.

### 4.5. High-pressure $CO_2$ and $CH_4$ sorption

Figs. 7 and 8 present the $CO_2$ and $CH_4$ sorption isotherms for all samples, respectively. The results indicate maximum excess sorption capacities for $CO_2$ ranging from 0.98 mmol/g to 1.25 mmol/g, and for $CH_4$ from 0.58 mmol/g to 0.74 mmol/g. Maximum excess sorption capacities decrease in the order of D6U1 > D6L6 > D6U5 > D6L3 > D6L2 for $CO_2$, and D6L6 > D6L3 > D6U1 > D6U5 > D6L2 for $CH_4$. All samples exhibit similar isotherm shapes, with maxima at approximately 6–8 MPa for $CO_2$, followed by a strong reduction, and at 15 MPa for $CH_4$, followed by a slight reduction. The fitted parameters for all isotherms are listed in Table 4. *nL* and *pL* values for $CO_2$ range between 1.37 and 3.12 mmol/g and 1.10 and 5.38 MPa, respectively. The values for $CH_4$ range from 0.96 to 1.29 mmol/g and 3.74–4.71 MPa, respectively.

A reduction in excess sorption for both $CO_2$ and $CH_4$ indicates that the densities of the volumetrically stored (free gas in the pore space) and sorptively stored (adsorbed) gas fractions are converging. When these densities become equal, the excess sorption approaches zero, as there is no longer a difference between the amount of gas stored by sorption and by simple pore filling. For $CO_2$, the pronounced decrease in excess sorption observed between 6 and 8 MPa pore pressure at 45°C is attributed to its transition into the supercritical phase. Above the critical temperature of 31.1°C and critical pressure of 7.38 MPa, $CO_2$ becomes supercritical, leading to a significant increase in its density. As a result, the density of the free (volumetrically stored) $CO_2$ in the pores approaches that of the adsorbed phase, causing the measured excess sorption to decrease sharply in this pressure range.

### 4.6. Free, adsorbed, and total $CH_4$ and $CO_2$ storage capacities

The skeletal ($\rho_s$) and bulk ($\rho_b$) density values and the corresponding porosity ($\phi$) and specific pore volume (SPV) values are presented in Table 5. Samples D6U1 and D6L2 have a significantly higher porosity compared to the remaining samples.

Free, adsorbed, and total $CH_4$ and $CO_2$ storage capacities are shown in Fig. 9. The storage capacities were calculated based on the assumption of typical pressure (hydrostatic pressure; 10 MPa $km^{-1}$) and temperature (30 °C $km^{-1}$) gradients in sedimentary basins. Adsorbed gas storage capacities were calculated using fitting parameters from the 3-parameter Langmuir fit (Table 4), and free gas storage capacities were calculated based on SPV values and gas density (Table 5). Finally, total gas storage capacities were obtained by summing up the free and adsorbed gas storage capacities. It should be noted that the effect of temperature on excess sorption capacity, as well as the effect of stress on both adsorptive and free gas storage capacities (e.g., [35]), were neglected.

## 5. Discussion

### 5.1. General coal characteristics

#### 5.1.1. Coal rank

Vitrinite reflectance (1.22 %Rr) classifies the investigated D6 coals as medium-volatile bituminous in rank, which is in good agreement with the measured $T_{max}$ values (average 466 °C). Sykes and Snowdon [73] suggested a series of plots based on Rock-Eval parameters to estimate the source potential and maturity of coals. The position of the D6 coals in these diagrams emphasizes the high rank beyond the threshold of the onset of gas generation (Fig. 10).

#### 5.1.2. Depositional environment

A detailed reconstruction of the depositional environment of the D6 seam is beyond the scope of the present work and is also hindered by its high rank. Nevertheless, ash yield and sulfur content of the D6 coal as well as maceral contents can be used as depositional environment indicators.

Ash yields and sulfur contents are considerably higher in low-lying (rheotrophic) mires than in (ombrotrophic) raised mires (e.g., [30,61, 24,31]). This is because raised mires develop above the regional (ground) water level and are protected from flooding by surface water due to their positive relief. These ecosystems rely solely on precipitation, which is deficient in sulfate and nutrients [14]. Humic acids exhibit poor dilution, resulting in raised mires being highly acidic, which inhibits bacterial activity. Raised-mire peat is thus characterized by very low levels of ash and sulfur, with well-preserved plant litter [12,16]. Furthermore, low-ash and low-sulfur coals may develop in freshwater low-lying mires in cases of limited detrital input [18]. In contrast, any brackish/marine influence will result in the formation of high-sulfur coal (>2 wt%).

Ash yields in coals derived from raised mires are typically below 4–6 wt% [31]. In the D6 seam, a limited number of coal samples exhibit ash yields below 6 wt% (Table 1), while most samples show higher values. This suggests deposition in a low-lying mire, although transitions to a raised mire cannot be excluded. Flooding events in the lower part of the seam increased ash yields significantly. The uniform and relatively low ash yield in the upper part of the seam reflects minor detrital input. A brackish/marine influence can be excluded based on the very low sulfur contents (<0.6 %) (Table 1).

High inertinite (e.g., fusinite) contents are indicative of subaerial oxidation and may be used as a proxy for dryness (e.g., [74]). Zieger and Littke [50] described the evolution of Carboniferous coal seams in the Ruhr Basin using the A/I ratio (=ash yield/[ash yield + fusinite]), where high and low values are characteristic for wet and dry conditions, respectively. The A/I trend for the D6 seam (Fig. 4) indicates a cyclic pattern with a general trend towards drier conditions during deposition of the upper part of the seam.

### 5.2. Low-pressure gas adsorption

#### 5.2.1. Isotherm characteristics

There is a hysteresis loop between the $N_2$ adsorption and desorption isotherms of the coal samples at $P/P_0$ values ranging from 0.45 to 1.0 (Fig. 5). This phenomenon indicates a delayed condensation of $N_2$ in mesopores (pore sizes between 2–50 nm), highlighting that capillary condensation and reverse evaporation of $N_2$ are distinct processes occurring at different relative pressures [56]. The lack of a final saturation plateau is attributed to condensation in macropores (pore sizes > 50 nm) and/or adsorption onto external surfaces in the samples, which facilitate unrestricted multilayer adsorption [33]. In general, the coals are categorized as mesoporous-to-macroporous [75] and the observed hysteresis loops are classified as Type H3 according to the IUPAC scheme. Such loops can arise from non-rigid clusters of plate-like particles, as well as from pore networks containing macropores that are not

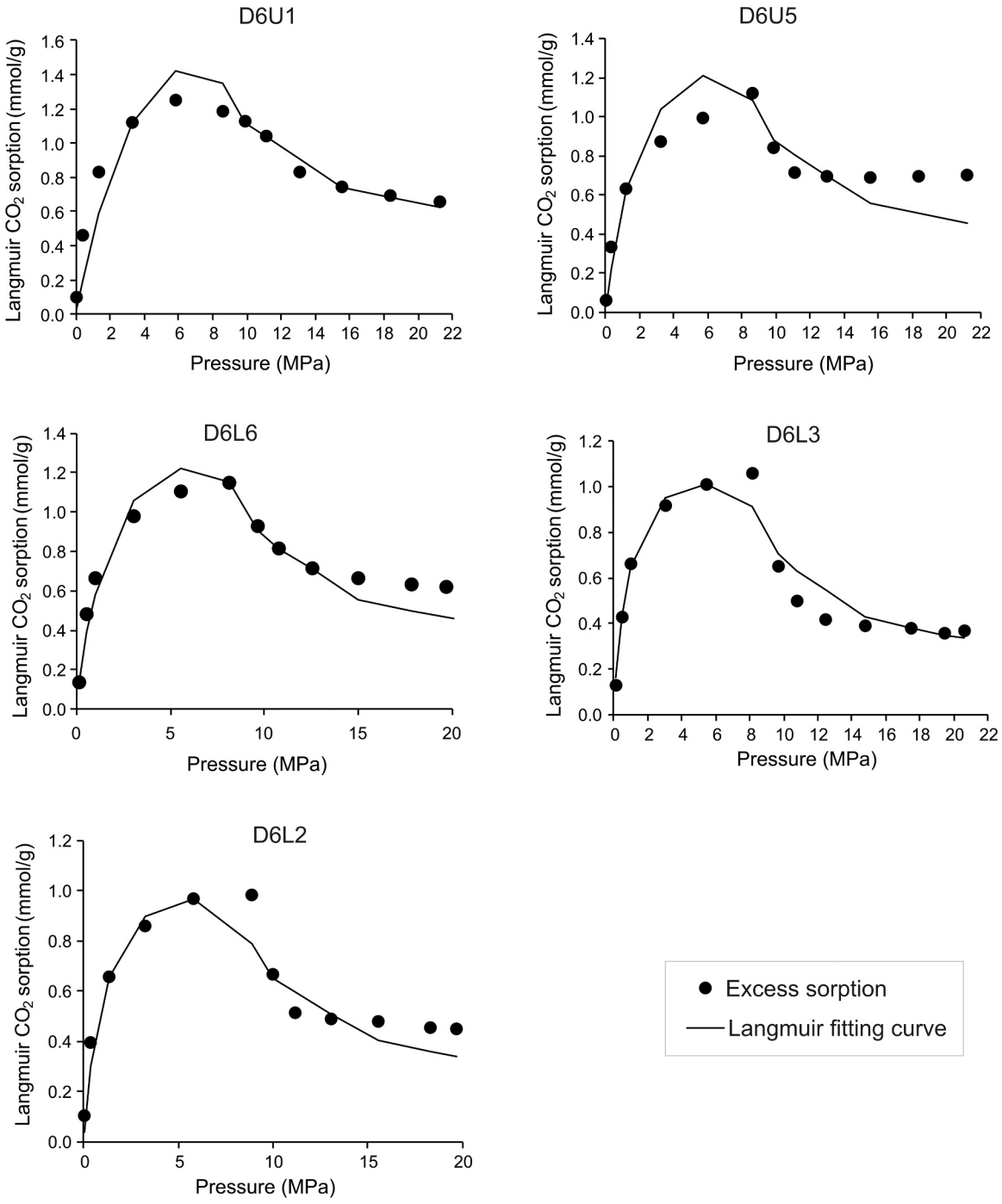


**Fig. 7.** Experimental HP $CO_2$ sorption data (recorded at 318 K) and the corresponding 3-parameter Langmuir fit of the samples.

entirely filled by pore condensate [75]. The lower limit of the desorption branch is generally observed at the cavitation-induced $P/P_0$ value of approximately 0.45 for this type [75].

*5.2.2. Impact of ash yield and TOC on low-pressure adsorption capacity*

There are strong positive correlations between ash yield, adsorbed $N_2$ volumes, and BET-SSA (Fig. 11a). This indicates that the mineral matter in the coals (e.g., clay minerals) is the main contributor to the internal surface area [46]. Previous studies indicated that mineral matter predominantly contributes to mesopores and macropores, while it can block micropores [46]. Considering that for the studied coals, a strong negative correlation between BET-SSA and $CO_2$ adsorption capacity (Fig. 11d) is observed, the decreasing proportion of available micropores may be related to the increasing ash yield causing micropore blockage.

Following the obvious negative correlation between ash yield and TOC content, BET-SSA and the resulting adsorbed $N_2$ volumes exhibit strong negative correlations with TOC (Fig. 11b). Instead, $CO_2$ exhibits a positive correlation (Fig. 11c) that is likely due to the comparably greater availability of organic matter and possibly enhanced physisorption/weak chemisorption processes associated with organic matter functional groups. Thus, it can be deduced that the $N_2$ adsorption capacity is greatly affected by the surface area of the inorganic component of the coals, while the $CO_2$ adsorption capacity depends on the abundance and type of organic matter (Fig. 11d).

With respect to micropore quantification, it is important to note that

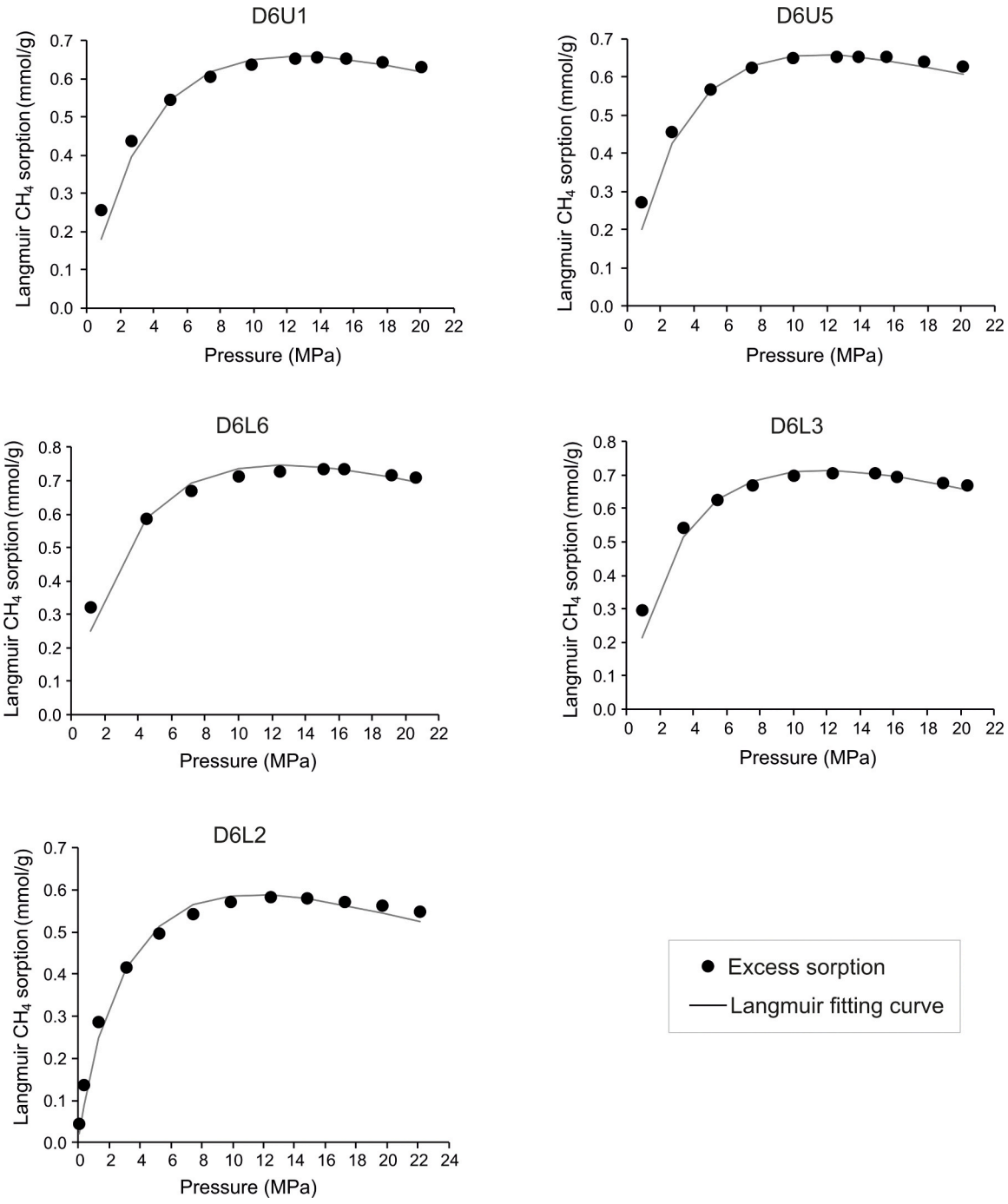


**Fig. 8.** Experimental HP $CH_4$ sorption data (recorded at 318 K) and the corresponding 3-parameter Langmuir fit of the samples.

**Table 4**
Maximum excess sorption data and Langmuir parameters obtained for $CO_2$ and $CH_4$.

| Sample | $nE_{CO2}$ | $nL_{CO2}$ | $pL_{CO2}$ | $nE_{CH4}$ | $nL_{CH4}$ | $pL_{CH4}$ |
|---|---|---|---|---|---|---|
| D6U1 | 1.25 | 3.12 | 5.38 | 0.66 | 1.14 | 4.68 |
| D6U5 | 1.12 | 2.05 | 2.80 | 0.65 | 1.08 | 3.85 |
| D6L6 | 1.15 | 1.94 | 2.25 | 0.74 | 1.29 | 4.71 |
| D6L3 | 1.06 | 1.37 | 1.10 | 0.71 | 1.18 | 4.00 |
| D6L2 | 0.98 | 1.37 | 1.40 | 0.58 | 0.96 | 3.74 |

nE: maximum excess sorption (mmol/g); nL: Langmuir capacity (mmol/g); pL: Langmuir pressure (MPa).

**Table 5**
Parameters used for the estimation of total $CO_2$ storage capacity (up to 20 MPa and 318 K).

| Sample | $\rho_s$ (g/cm$^3$) | $\rho_b$ (g/cm$^3$) | φ | SPV (cm$^3$/g) |
|---|---|---|---|---|
| D6U1 | 1.43 | 1.22 | 0.15 | 0.12 |
| D6U5 | 1.36 | 1.21 | 0.11 | 0.09 |
| D6L6 | 1.35 | 1.27 | 0.06 | 0.05 |
| D6L3 | 1.33 | 1.26 | 0.05 | 0.04 |
| D6L2 | 1.39 | 0.98 | 0.30 | 0.31 |
| Average | 1.37 | 1.19 | 0.13 | 0.12 |

$\rho_s$: skeletal density; $\rho_b$: bulk density; φ: porosity (1- $\rho_b/\rho_s$); SPV: specific pore volume ($\varphi/\rho_b$).

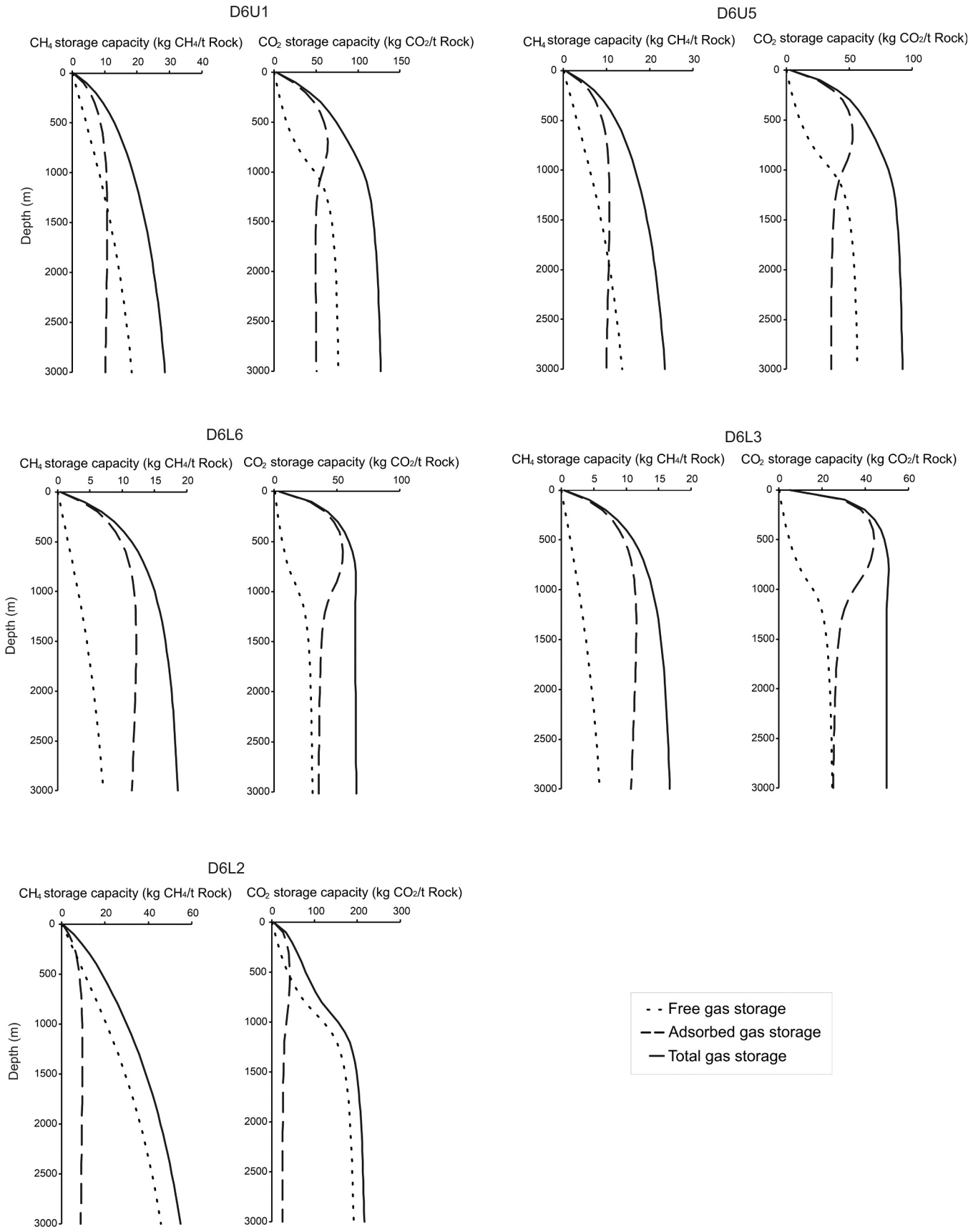


**Fig. 9.** Variation of free, adsorbed, and total $CH_4$ and $CO_2$ storage capacities of the studied coals with depth.

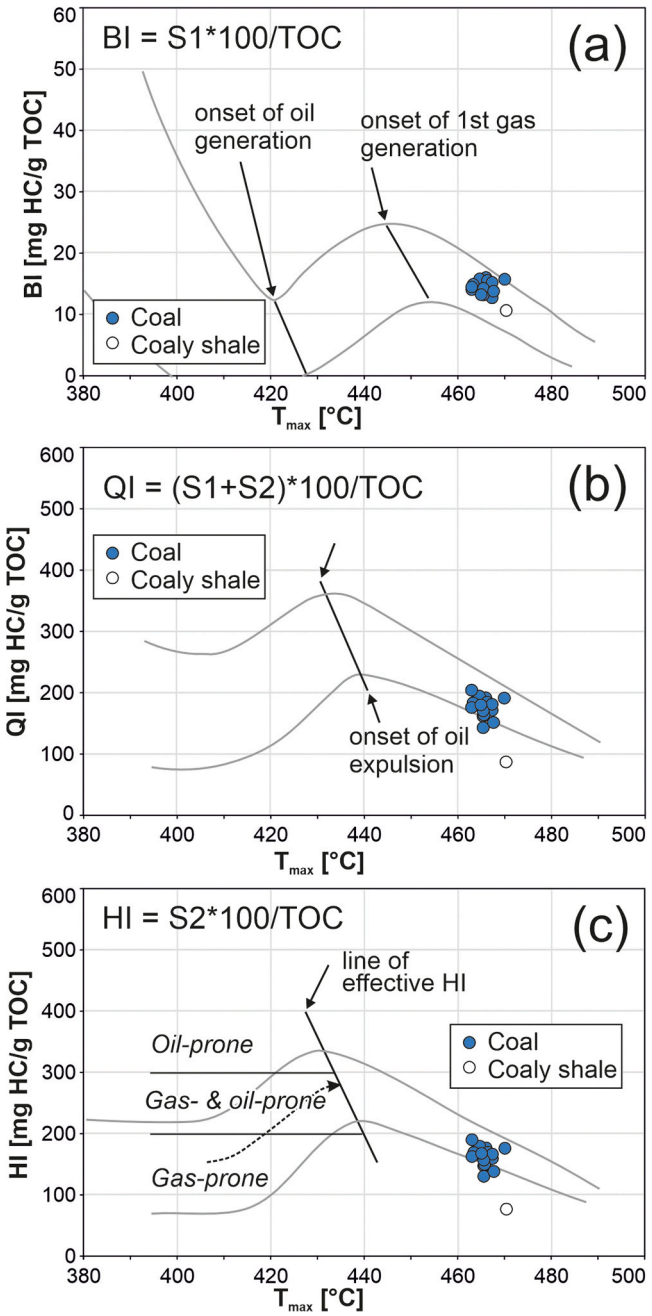


**Fig. 10.** Position of D6 samples in plots of $T_{max}$ versus (a) bitumen index (BI), (b) quality index (QI) and (c) hydrogen index (HI). Plots after Sykes and Snowdon [73].

the investigated coal samples do not indicate significant adsorbed volumes of $N_2$ at $P/P_0$ of ~0.01. Additionally, the statistical thickness (t-plot) method was applied to the $N_2$ adsorption data [69], resulting in estimated micropore volume and surface area values as being zero. However, literature reports high proportions of ultra-micropores (<0.7 nm) in coals (e.g., [5]). Brouwer et al. [8] also suggested that ultra-micropores can be accurately quantified solely through $CO_2$ adsorption isotherms, while $N_2$ adsorption is limited to measuring "super-micropores" (0.7–2.0 nm) and may lead to an underestimation of micropore volume. This has been attributed to the insufficient adsorption energy of $N_2$ molecules preventing their entry into ultra-micropores at cryogenic temperatures (77 K) [5]. Therefore, it may be hypothesized that ultra-micropores exist in the samples, which were undetectable by $N_2$ data but contribute to $CO_2$ storage capacity. Nevertheless, as will be discussed in the following sections, the process of $CO_2$ sorption in the studied coals is not fully reversible, most probably, due to enhanced physisorption/weak chemisorption of $CO_2$ within coal. Thus, the possible occurrence of ultra-micropores in the coals could be unrealistic and related to artifacts.

Additionally, according to the high rank of the coal samples (mean % Rr = 1.22), it can be assumed that bituminization has occurred in the coals. Thus, blockage of the micropores in the samples by the generated bitumen may be significant [51,77,83]. Another potential reason for the absence of micropores in the studied coals may be the blockage of these micropores by minerals [84]. This is indicated for the sample set studied here by the negative correlation of LP-$CO_2$ adsorption capacity with ash yield and consequently BET-SSA (Fig. 11c,d).

### 5.3. *High-pressure $CO_2$ and $CH_4$ sorption*

#### 5.3.1. *Isotherm characteristics*

Enhanced physisorption/weak chemisorption processes associated with organic matter functional groups are likely responsible for the significant $CO_2$ sorption capacity of the studied coals at low pressures (Fig. 7).

The comparison of nL values for $CO_2$ and $CH_4$ (Table 4) shows a greater affinity for $CO_2$, as documented in the literature (e.g., [11,17,27,86]). $CO_2$'s higher adsorption affinity is due to its larger molecular weight, smaller kinetic diameter (0.33 nm vs. 0.38 nm for $CH_4$), and its linear configuration, which allows it to penetrate narrower pores [21,36]. Additionally, $CO_2$'s quadrupole moment and high electronegativity result in a strong attractive force with the coal surface [57,9].

#### 5.3.2. *Impact of ash yield and TOC on HP adsorption capacity*

Fig. 12a-c depicts the effect of ash yield, TOC, and BET-SSA on nL-$CH_4$ and nL-$CO_2$. For $CH_4$, a higher TOC content substantially enhances the adsorption capacity, while a higher ash yield notably decreases it (Fig. 12a).

In contrast to observations from LP tests for subcritical $CO_2$, ash yield and TOC do not significantly affect nL-$CO_2$ (Fig. 12b). Additionally, no obvious correlation between nL-$CO_2$ and BET-SSA is seen (Fig. 12c). This may suggest that under HP conditions, supercritical $CO_2$ can be adsorbed in larger pores (e.g., mesopores), differing from its behavior in the subcritical state (Fig. 12c,d). Although some studies discuss a potential interaction between supercritical $CO_2$ and mineral matter including carbonate and clay minerals [44,71,79,81], the low calcite equivalent percentages (Table 1) and the minor sensitivity of adsorption capacity to ash yield and BET-SSA (Fig. 12) suggest a negligible influence of mineral matter composition on HP adsorption behavior. Another possible reason for lack of the correlations between nL-$CO_2$ and ash yield and TOC could be the high sensitivity of $CO_2$ at critical point. This may act as a potential source of error in the sorption values measured.

### 5.4. *$CO_2$ adsorption-desorption hysteresis*

Recording $CO_2$ desorption isotherms for all samples at LP and for one selected sample at HP conditions revealed a hysteresis between adsorption and desorption pathways (Figs. 13,14). At LP conditions, the adsorbed $CO_2$ molecules are completely desorbed at the end of the desorption process. Thus, despite the existence of a hysteresis loop, the process of $CO_2$ adsorption is fully reversible (Fig. 13).

$CO_2$ adsorption-desorption hysteresis has been observed in some previous studies on coals (e.g., [15,62,65]), and various potential causes including capillary condensation [13], presence of ink-bottle-shaped pores [29], presence of volatile matter at pore throats [5], as well as effects of residual moisture [32], have been suggested. However, the most likely mechanism responsible for the creation of a hysteresis at LP conditions are electrostatic interactions between the injected $CO_2$ and surface functional groups associated with the organic matter fraction in coals. These interactions have been documented in previous studies [2,

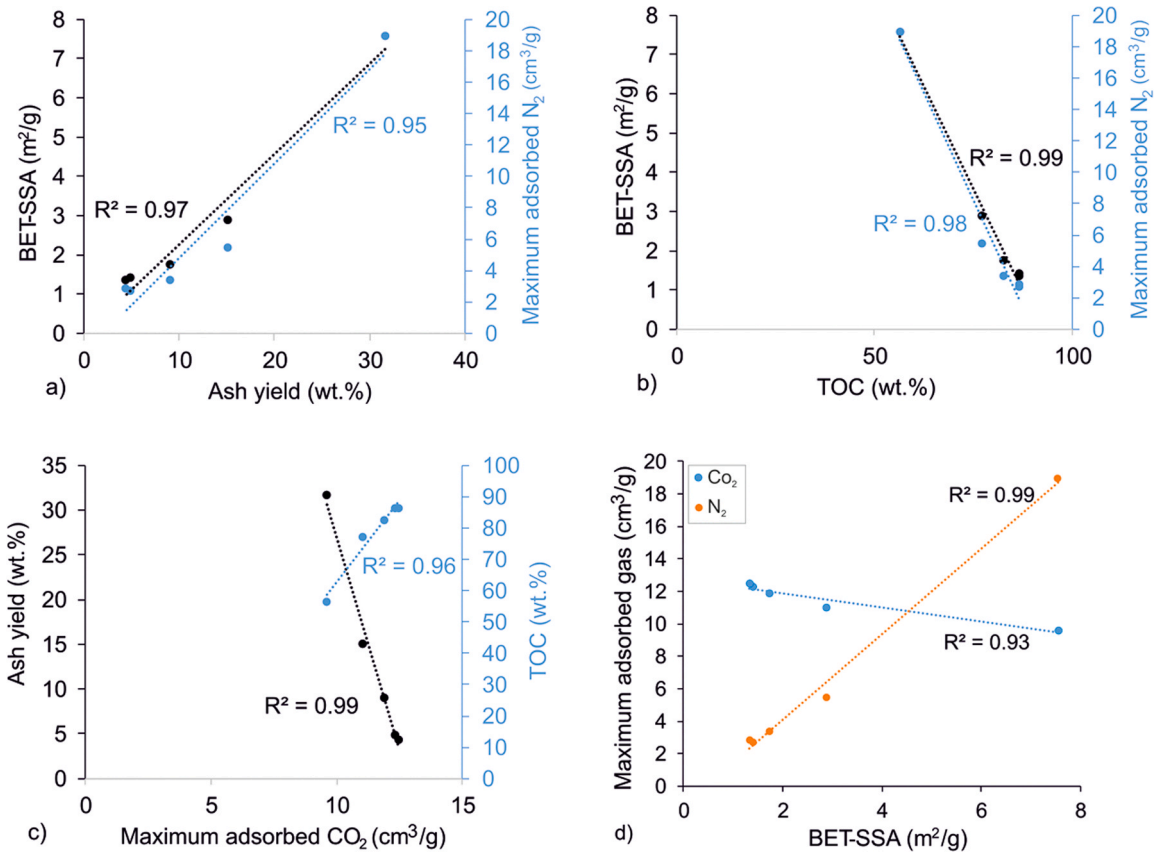


**Fig. 11.** Correlation plots between the ash yield and BET-SSA and $N_2$ adsorbed volume (a), TOC content and BET-SSA and $N_2$ adsorbed volume (b), the ash yield and TOC content and $CO_2$ adsorbed volume (c), and BET-SSA and adsorbed volumes of $CO_2$ and $N_2$ during LP measurements (d).

25,66] and it has been shown that the resulting electrostatic forces can be stronger than van der Waals forces [52,55,67], enhancing the $CO_2$ adsorption capacity. As van der Waals forces are the main controlling factor for physisorption [55], it can be inferred that an enhancement beyond pure physisorption (i.e., enhanced physisorption or weak chemisorption) occurs during LP $CO_2$ sorption, causing the adsorption-desorption hysteresis.

In contrast to LP tests, the hysteresis between $CO_2$ adsorption and desorption recorded at HP conditions (Fig. 14) indicates that HP adsorption is partly irreversible. This means that even at very low pressures in the final stage of desorption, some of the $CO_2$ remains trapped and cannot be fully desorbed. The establishment of hydrogen bonds between supercritical $CO_2$ and polar functional groups in organic matter, subsequently leading to chemisorption [15,80], as well as matrix swelling and shrinkage [78], could be the primary causes of the partial irreversibility of $CO_2$ HP sorption. This suggests that hydrogen bonding only occurs under high-pressure conditions, where $CO_2$ molecules are in supercritical phase, and not at low-pressure conditions, where $CO_2$ molecules are in subcritical phase.

It is worth noting that the observed hysteresis is generally advantageous for storage purposes as it shows that the injected $CO_2$ will remain safely trapped even in case of a reservoir pressure decrease, e.g. caused by tectonic uplift or changes in pore pressure due to other subsurface operations.

### 5.5. CCS and $CO_2$-ECBM potentials of the D6 seam

The $CO_2$-ECBM potential and resulting CCS capacity of the D6 seam in the Dolin Formation were calculated using Eqs. 7 to 9 and applying an RF of 0.4 and a CF value of 0.1 as used by Hendriks et al. [34] and Weniger et al. [81].

The areal extent of the D6 seam applying an upper depth cut-off of 800 m is estimated as 40 $km^2$. The average thickness of the seam is assumed as 5.5 m according to available mining data. Laboratory measurements yielded an average coal density of 1.37 $t/m^3$ . Based on these parameters, the total mass of coal in the D6 seam is calculated at 301,400,000 (~ 300 million tons) and the corresponding coal volume at 220 million $m^3$ .

According to the average supercritical $CH_4$ excess sorption capacity, the mean gas content of the D6 coal seam is 0.65 mmol/g (14.66 $m^3/t$). However, significantly higher gas contents (~ 30–32 $m^3/t$) have been observed during coal exploitation at 600–900 m depth. The discrepancy between the theoretical and the measured gas content may be in part to free gas (e.g., in cleat systems) or to gas stored in the rocks above and below the seam. Accepting a gas content of 30 $m^3$ /t, the initial gas in place (IGIP) is estimated as 9042,000,000 $m^3$ (~ 9 billion $m^3$). With an RF of 0.4 and a CF of 0.1, the producible gas in place (PGIP), which represents the $CO_2$-ECBM potential of the D6 seam in the area, is calculated at 361,680,000 $m^3$ (~ 360 million $m^3$).

For the assessment of the resulting CCS potential by adsorption, the exchange ratio (ER) between $CO_2$ and $CH_4$ is important. The maximum Langmuir ($n_L$) $CO_2$ and $CH_4$ adsorption data from D6 samples (Table 4) indicate a mean ER of 2.05. However, Liu et al. [54] showed that the measurement of the exchange ratio of $CO_2$ and $CH_4$ in coal based on pure gas measurements leads to an underestimation of ER, as the effect of competitive sorption is neglected. Using mixed-gas experiments, Liu et al. [54] showed that the actual selectivity of $CO_2$ over $CH_4$ adsorption in coal is 1.5–2.5 times higher than the ratio determined based on a comparison of measurements with pure gases. Based on these findings and considering a conservative increase of 1.5 times, a modified ER value of 3.07 is used in the present study.

To assess the CCS potential of the D6 seam, two approaches have

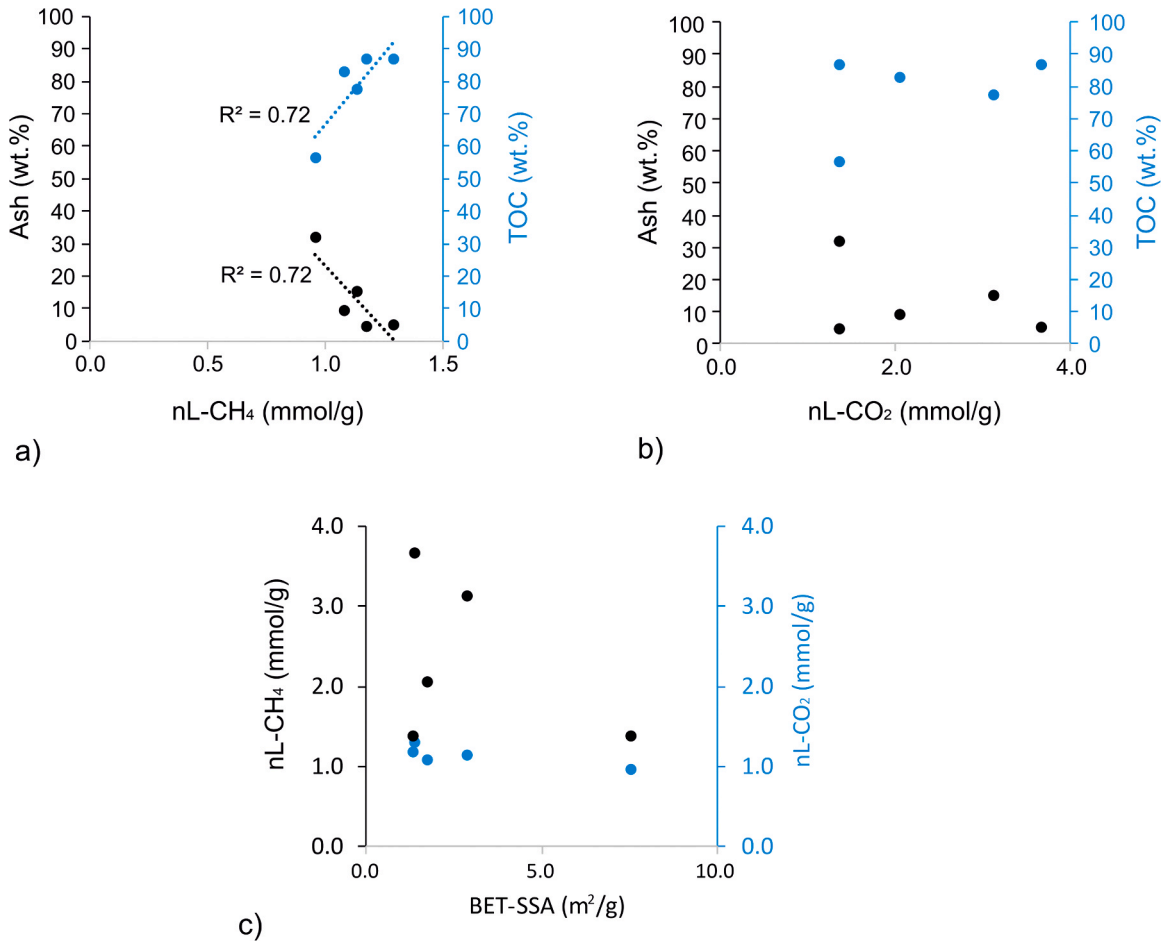


**Fig. 12.** The impact of ash yield, TOC content, and BET-SSA on Langmuir $CH_4$ and $CO_2$ sorption capacities.

been used. First, the average Langmuir sorption capacity below 800 m (39.02 kg/t [Fig. 9]; corresponding to 18.57 $m^3$/t and 0.83 mmol/g), corrected for the moisture content of the coal, was used to calculate the adsorptive storage capacity. The moisture content of the D6 coal ranges from 0.8 to 0.9 wt% (e.g., [68]). Considering the molar mass of $H_2O$ (18.015 g/mol), the seam contains nearly 0.5 mmol $H_2O$ per gram of coal. Busch and Gensterblum [10] suggested that in bituminous coal, each water molecule displaces ~0.3 molecules of $CO_2$. Consequently, the moisture content reduces the $CO_2$ adsorption capacity by 0.15 mmol/g, from 0.83 to 0.68 mmol/g (15.24 $m^3$/t). By adopting this value in Eq. 7 (for GC) and Eq. 8 (for PGIP) and applying Eq. 9, the adsorptive CCS potential is estimated at 1.1 Gt.

In the second approach, the total storage capacity below 800 m (96.64 kg/t; 48.88 $m^3$/t, Fig. 9), including additional volume filling of pores by free, supercritical $CO_2$, was considered. Again, by adopting the values in Eq. 7 (for GC) and Eq. 8 (for PGIP) and using Eq. 9, the total CCS potential is estimated at 3.6 Gt.

It should be emphasized that the calculations in this study are based on conservative estimates for the efficiency factors RF and CF. Even though the calculations are simple static potential estimates, they show that the storage capacity of the D6 seam is substantial and significantly higher than the storage capacity calculated for depleted oil and gas deposits in Kazakhstan (1.2 Gt; [3]). The determined total storage capacity of the D6 seam alone (3.6 Gt) would be sufficient to store the annual $CO_2$ emissions in Kazakhstan (~255 mio. t in 2023; [28]) for 14 years. Similar storage capacities are expected for coal seams in the Karaganda Formation. This shows that CCS in deeply buried coal seams is a highly promising technique for decarbonization of hard-to-abate industry and energy sectors in Kazakhstan.

## 6. Conclusions

The Upper Carboniferous D6 seam, a major coal resource in the Karaganda Basin, was characterized in detail with respect to bulk geochemical and compositional parameters, as well as its rank. The main study aim was then to assess its CCS and $CO_2$-ECBM potential by LP and HP gas adsorption tests. The most important findings regarding depositional environment, resource and storage potential are summarized below:

- The D6 seam in the Lenin mine reached the medium-volatile bituminous coal rank.
- Variable, but locally relatively high ash yields together with very low sulfur contents suggest deposition in a low-lying mire without a brackish/marine influence. Upward increasing fusinite contents suggest increasingly drier conditions during proceeding peat accumulation.
- LP $N_2$ adsorption measurements classify the coals as mesoporous-to-macroporous with BET-SSA and BJH-SPV ranging from 1.33 to 7.55 $m^2$/g and 0.004–0.028 $cm^3$/g, respectively.
- The average selectivity of $CO_2$ over $CH_4$ under HP conditions was calculated at 2.05.
- At LP conditions, $CO_2$ adsorption capacity increases with increasing TOC content, but decreases with increasing mineral matter content (ash yield). However, under HP conditions, the effect of TOC and ash yield on $CO_2$ adsorption capacity is minor. In contrast, $CH_4$ HP adsorption increases considerably with increasing TOC content.
- The observed hysteresis loop at LP conditions may result from electrostatic interactions between the injected $CO_2$ and surface

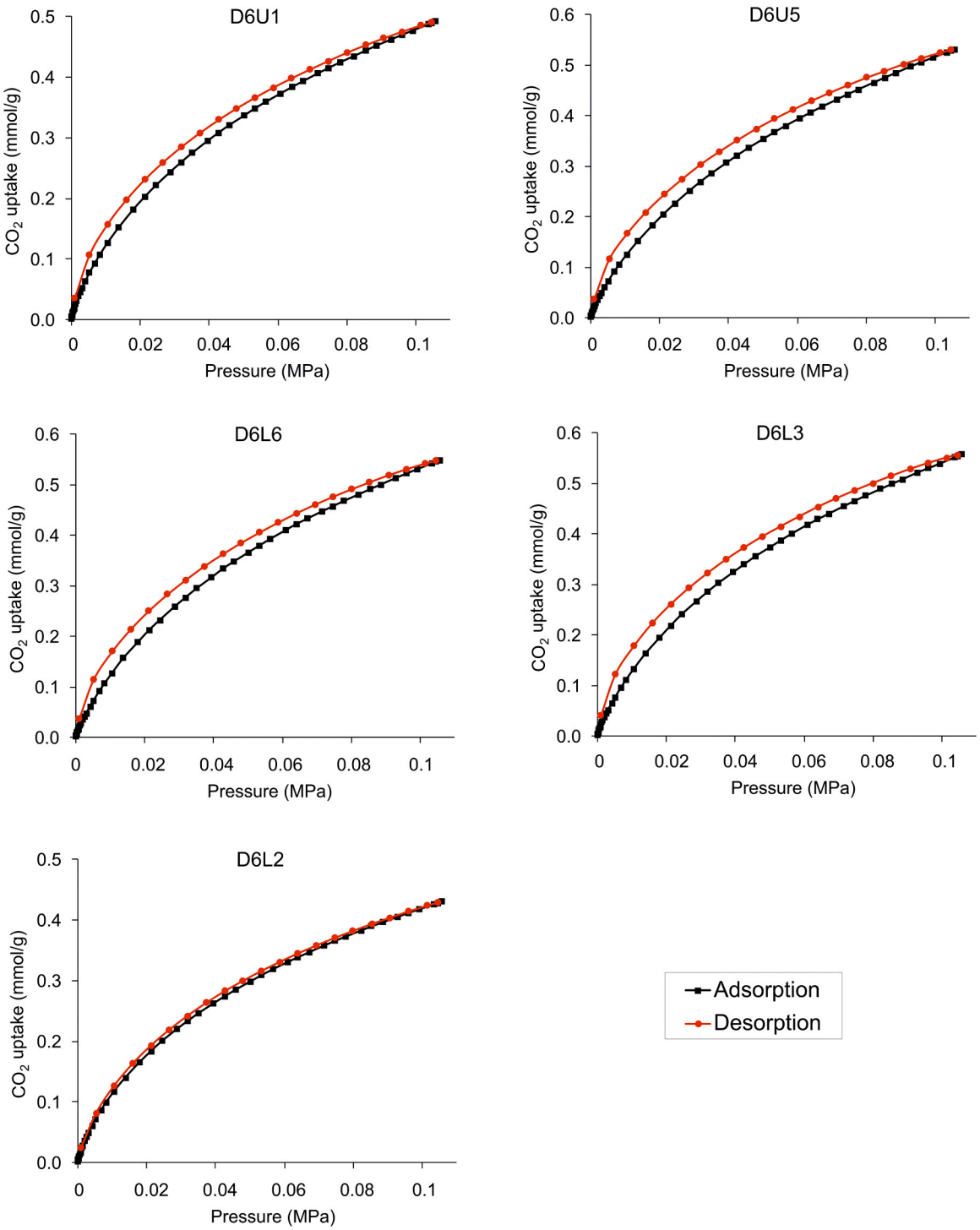


**Fig. 13.** $CO_2$ adsorption-desorption isotherms of the samples recorded at 273 K and up to 0.1 MPa.

functional groups in the organic matter fraction leading to an enhanced physisorption.

- The observed hysteresis loop at HP conditions may result from $CO_2$ chemisorption and coal matrix swelling and shrinkage. This behavior is beneficial to storage safety as it suggests stable adsorption even in case of a reservoir pressure reduction.
- The CBM potential of the D6 seam is estimated at 9 billion $m^3$ initial gas in place and 360 million $m^3$ producible gas in place.
- The total $CO_2$ storage capacity during $CO_2$-ECBM operations is estimated at 3.6 Gt.

Using the D6 seam as an example, this study shows that coal seams in the Karaganda Basin have very high $CO_2$-ECBM and CCS potential. According to the theoretical total storage capacity estimation, the D6 seam alone has the potential to sequester Kazakhstan's current annual $CO_2$ emissions for 14 years. Detailed reservoir development simulations need to confirm if this storage resource can be tapped by the hard-to-abate industry emitters in the region.

## CRediT authorship contribution statement

**Milovan Fustic:** Writing – review & editing, Investigation,

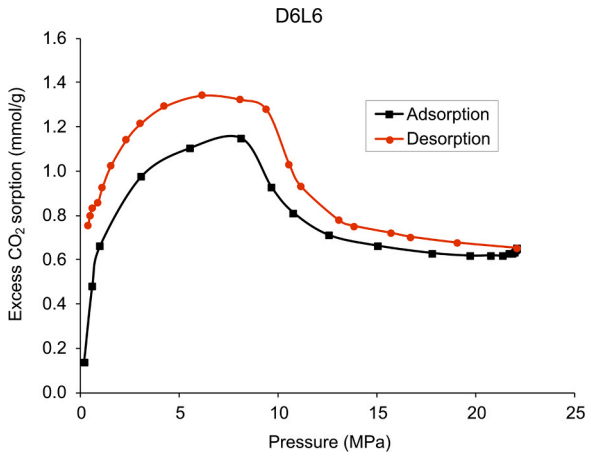


**Fig. 14.** Excess $CO_2$ adsorption-desorption isotherms (318 K) for the selected sample (D6L6).

Conceptualization. **Thorsten Bauersachs:** Writing – review & editing, Investigation. **Medet Junussov:** Investigation. **Nikolaos Kostoglou:** Writing – review & editing, Resources, Investigation, Formal analysis. **Garri Gaus:** Writing – review & editing, Investigation, Formal analysis. **David Misch:** Writing – review & editing, Validation, Supervision, Investigation, Conceptualization. **Sachsenhofer Reinhard:** Writing – review & editing, Validation, Investigation, Conceptualization. **Safaei Farouji Majid:** Writing – original draft, Methodology, Investigation, Formal analysis, Data curation.

## Declaration of Competing Interest

The authors declare no competing interests.

## Acknowledgements

The authors thank staff members from the Lenin Mine for permission to sample the D6 seam during their underground mining operations. Drs. Svetlana Nikolaeva (Natural History Museum, London, UK) and Fandus Mullagaliyev (Karaganda Technical University, Kazakhstan) are sincerely thanked for useful discussions about the stratigraphy of the Karaganda basin. Work of David Misch was supported by the Austrian Science Fund FWF grant no.: P 33883 and work of Milovan Fustic was supported by Nazarbayev University (grant no. 111024CRP2015). Nikolaos Kostoglou is grateful to Oskar Paris from Montanuniversität Leoben for providing access to the low-pressure gas sorption analyzer.

## Data availability

Data will be made available on request.

## References

[1] Matveev, A.K. (ed.), 1990. Geology of coal deposits of the USSR. Moscow University Press, 352.
[2] M. Abunowara, M.A. Bustam, S. Sufian, M. Babar, U. Eldemerdash, A. Mukhtar, S. Ullah, M.A. Assiri, A.G. Al-Sehemi, S.S. Lam, High pressure $CO_2$ adsorption onto Malaysian Mukah-Balingian coals: adsorption isotherms, thermodynamic and kinetic investigations, Environ. Res. 218 (2023) 114905.
[3] Y. Abuov, N. Seisenbayev, W. Lee, $CO_2$ storage potential in sedimentary basins of Kazakhstan, Int. J. Greenh. Gas. Control 103 (2020) 103186, https://doi.org/10.1016/j.ijggc.2020.103186.
[4] ASTM D3174, 2012. Standard Test Method for Ash in the Analysis Sample of Coal and Coke from Coal, 6.
[5] J.S. Bae, S.K. Bhatia, V. Rudolph, P. Massarotto, Pore accessibility of methane and carbon dioxide in coals, Energy Fuels 23 (2009) 3319–3327.
[6] S. Baimukhametov, Y. Stefluk, M.D. Velzeboer, Development and mining of high gas low permeability coal seams in the karaganda coal field-Kazakhstan, 12th coal operators, in: Conference, University of Wollongong & The Australasian Institute of Mining and Metallurgy, 2012, 2012, pp. 260–267.
[7] Bakitovna, I.S., 2022. Study of the influence of mining and geological conditions of D6 bed occurrence and its methane content on the efficiency of mining operations. PhD thesis, Karaganda Technical University, 156 pp.
[8] S. Brouwer, J.C. Groen, L.A.A. Peffer, The impact of mesoporosity on microporosity assessment by $CO_2$ adsorption, revisited, Stud. Surf. Sci. Catal. 160 (2007) 145–152, https://doi.org/10.1016/S0167-2991(07)80020-6.
[9] A.D. Buckingham, R.L. Disch, The quadrupole moment of the carbon dioxide molecule, Proc. R. Soc. A 273 (1963) 275–289, https://doi.org/10.1098/rspa.1963.0088.
[10] A. Busch, Y. Gensterblum, CBM and CO2-ECBM related sorption processes in coal: a review, Int. J. Coal Geol. 87 (2011) 49–71.
[11] A. Busch, Y. Gensterblum, B.M. Krooss, Methane and $CO_2$ sorption and desorption measurements on dry argonne premium coals: pure components and mixtures, Int. J. Coal Geol. 55 (2003) 205–224, https://doi.org/10.1016/S0166-5162(03)00113-7.
[12] C.C. Cameron, J.S. Esterle, C.A. Palmer, The geology, botany and chemistry of selected peat-forming environments from temperate and tropical latitudes, Int. J. Coal Geol. 12 (1989) 105–156.
[13] J. Chen, F. Wang, H. Liu, H. Wu, Molecular mechanism of adsorption/desorption hysteresis: dynamics of shale gas in nanopores, Sci. China Phys. Mech. Astron 60 (2017) 1–8.
[14] R.S. Clymo, The ecology of peatlands, Sci. Prog. Oxf. 71 (1987) 593–614.
[15] K. Czerw, P. Baran, J. Szczurowski, K. Zarębska, Sorption and desorption of CO 2 and CH 4 in Vitrinite-and Inertinite-Rich polish Low-Rank coal, Nat. Resour. Res. 30 (2021) 543–556.
[16] S. Dai, A. Bechtel, C.F. Eble, R.M. Flores, D. French, I.T. Graham, M.M. Hood, J. C. Hower, V.A. Korasidis, T.A. Moore, W. Puttman, Q. Wei, L. Zhao, J.M. K. O'Keefe, Recognition of peat depositional environments in coal: a review, Int. J. Coal Geol. 219 (2020) 103383.
[17] S. Day, R. Sakurovs, S. Weir, Supercritical gas sorption on moist coals, Int. J. Coal Geol. 74 (2008) 203–214.
[18] Diessel, C.F.K., 1992. Coal-Bearing Depositional Systems. Springer Berlin, Heidelberg.
[19] N.A. Drizhd, R.K. Kamarov, D.R. Akhmatnurov, N.M. Zamaliyev, I.M. Shmidt-Fedotova, Coal Bed Methane of Karaganda Basin in the Gas Balance of the Republic of Kazakhstan: Status and Prospects, Naukovyi Visnyk Natsionalnoho Hirnychoho Universytetu 2017 (2017) 12–20.
[20] X. Du, Y. Cheng, Z. Liu, H. Yin, T. Wu, L. Huo, C. Shu, $CO_2$ and $CH_4$ adsorption on different rank coals: a thermodynamics study of surface potential, gibbs free energy change and entropy loss, Fuel 283 (2021) 118886.
[21] S. Duan, M. Gu, X. Du, X. Xian, Adsorption equilibrium of $CO_2$ and $CH_4$ and their mixture on sichuan basin shale, Energy Fuels 30 (2016) 2248–2256, https://doi.org/10.1021/acs.energyfuels.5b02088.
[22] U.S. Environmental Protection Agency, 2011. Deep Gassy Coal Mines of Karaganda Coal Basin.
[23] J. Espitalie, M. Madec, B. Tissot, J.J. Mennig, P. Leplat, Source rock characterization method for petroleum exploration, Offshore Technol. Conf. (1977), https://doi.org/10.4043/2935-MS.
[24] H.N. Fikri, R.F. Sachsenhofer, A. Bechtel, D. Gross, Coal deposition in the barito basin (Southeast Borneo): the eocene tanjung formation compared to the miocene warukin formation, Int. J. Coal Geol. 263 (2022) 104117, https://doi.org/10.1016/j.coal.2022.104117.
[25] E. Gabruś, K. Wojtacha-Rychter, T. Aleksandrzak, A. Smoliński, M. Król, The feasibility of CO2 emission reduction by adsorptive storage on polish hard coals in the upper silesia coal basin: an experimental and modeling study of equilibrium, kinetics and thermodynamics, Sci. Total Environ. 796 (2021) 149064.
[26] Gašparík, M., 2013. Experimental investigation of gas storage properties of black shales (Doctoral dissertation, Aachen, Techn. Hochsch., Diss., 2013).
[27] Y. Gensterblum, A. Merkel, A. Busch, B.M. Krooss, High-pressure CH4 and CO2 sorption isotherms as a function of coal maturity and the influence of moisture, Int. J. Coal Geol. 118 (2013) 45–57.
[28] Global Carbon Budget, 2024. – with major processing by Our World in Data. "Cumulative $CO_2$ emissions – GCB" [dataset]. Global Carbon Project, "Global Carbon Budget" [original data]. Retrieved Jan. 21, 2025 from ⟨https://ourworldindata.org/grapher/cumulative-co-emissions⟩.
[29] A.L. Goodman, A. Busch, G.J. Duffy, J.E. Fitzgerald, K.A.M. Gasem, Y. Gensterblum, B.M. Krooss, J. Levy, E. Ozdemir, Z. Pan, R.L. Robinson, An inter-laboratory comparison of $CO_2$ isotherms measured on argonne premium coal samples, Energy Fuels 18 (2004) 1175–1182.
[30] W. Gruber, R.F. Sachsenhofer, Coal deposition in the noric depression (Eastern Alps): raised and low-lying mires in miocene pull-apart basins, Int J. Coal Geol. 48 (2001) 89–114, https://doi.org/10.1016/S0166-5162(01)00049-0.
[31] Q. Guo, R. Littke, L. Zieger, Petrographical and geochemical characterization of sub-bituminous coals from mines in the Cesar-Ranchería basin, Colombia, Int. J. Coal Geol. 191 (2018) 66–79.
[32] S. Harpalani, B.K. Prusty, P. Dutta, Methane/CO2 sorption modeling for coalbed methane production and CO2 sequestration, Energy Fuels 20 (2006) 1591–1599.
[33] X. He, Y. Cheng, B. Hu, Z. Wang, C. Wang, M. Yi, L. Wang, Effects of coal pore structure on methane-coal sorption hysteresis: an experimental investigation based on fractal analysis and hysteresis evaluation, Fuel 269 (2020) 117438.
[34] Hendriks, C., Graus, W., van Bergen, F., 2004. Global carbon dioxide storage potential and costs. Ecofys-report EEP-02001. 59. ⟨http://www.ecofys.com/com/publications/documents/GlobalCarbonDioxideStorage.pdf⟩, (Accessed 6 December 2009).

[35] S. Hol, Y. Gensterblum, P. Massarotto, Sorption and changes in bulk modulus of coal—experimental evidence and governing mechanisms for CBM and ECBM applications, Int. J. Coal Geol. 128 (2014) 119–133.
[36] K. Huang, X. Du, K. Li, J. Zhou, D. Zhang, N. Abbas, Y. Cheng, T. Wu, G. Liu, Cs He, Competitive adsorption of CO2/CH4 on coal: insights from thermodynamics, Alex. Eng. J. 97 (2024) 114–126.
[37] ICCP (International Committee for Coal and Organic Petrology), The new vitrinite classification (ICCP system 1994, Fuel 77 (5) (1998) 349–358, https://doi.org/10.1016/S0016-2361(98)80024-0.
[38] ICCP (International Committee for Coal and Organic Petrology), The new inertinite classification (ICCP system 1994, Fuel 80 (4) (2001) 459–471, https://doi.org/10.1016/S0016-2361(00)00102-2.
[39] International energy Agency (IEA), Kazakhstan 2022 Energy Sector Review, 2022.
[40] ISO 7404-2, 2009. Methods for the Petrographic Analysis of Coals - Part 2: Methods of Preparing Coal Samples 7404–2. ⟨https://www.iso.org/standard/42798.html⟩.
[41] ISO 7404-3, 2009. Methods for the petrographic analysis of coals - Part 3: Method of determining maceral group composition, Standards Australia, Level 10, The Exchange Centre 20 Bridge Street, GPO Box 476, AU-Sydney NSW 2001. ⟨www.standards.org.au⟩.
[42] ISO 7404-5, 2009. Methods for the Petrographic Analysis of Coals - Part 5: Method of Determining Microscopically the Reflectance of Vitrinite 7404–5. ⟨https://www.iso.org/standard/42832.html⟩.
[43] O. Ivakhnenko, A. Aimukhan, A. Kenshimova, F. Mullagaliyev, E. Akbarov, L. Mullagaliyeva, S. Kabirova, A. Almukhametov, Advances in coalbed methane reservoirs integrated characterization and hydraulic fracturing for improved gas recovery in karaganda coal basin, Kazakhstan, Energy Procedia 125 (2017) 477–485.
[44] R. Jiang, H. Yu, Interaction between sequestered supercritical CO2 and minerals in deep coal seams, Int. J. Coal Geol. 202 (2019) 1–13.
[45] K. Jin, Y. Cheng, Q. Liu, W. Zhao, L. Wang, F. Wang, D. Wu, Experimental investigation of pore structure damage in pulverized coal: implications for methane adsorption and diffusion characteristics, Energy Fuels 30 (2016) 10383–10395.
[46] A.I. Karayiğit, R.G. Oskay, Y. Bulut, M. Mastalerz, Meso-and microporosity characteristics of miocene ligniteand subbituminous coals in the Kınık coalfield (Soma Basin, W. Turkey), Int. J. Coal Geol. 232 (2020) 103624.
[47] V.V. Korobkin, M.M. Buslov, Tectonics and geodynamics of the Western central asian fold belt (Kazakhstan Paleozoides), Russ. Geol. Geophys. 52 (2011) 1600–1618.
[48] O. Kunz, W. Wagner, The GERG-2008 wide-range equation of state for natural gases and other mixtures: an expansion of GERG-2004, J. Chem. Eng. Data 57 (11) (2012) 3032–3091.
[49] Kuznetsova, E., Vaillancourt, K., 2023. Energy Transition in Monocities. Coal Phase-out Roadmap and Just Transition Action Plan for Ekibastuz (Kazakhstan).
[50] L. Zieger, R, Littke, Bolsovian (Pennsylvanian) tropical peat depositional environments: the example of the Ruhr Basin, Germany, International Journal of Coal Geology 211 (2019) 103209.
[51] J.R. Levine, Coalification: the evolution of coal as source rock and reservoir rock, in: B.E. Law, D.D. Rice (Eds.), Hydrocarbons from Coal. Am. Assoc. Pet. Geol. Stud. Geol, 38, American Association of Petroleum Geologists, Tulsa, OK, 1993, pp. 39–77.
[52] Z. Li, C. Ding, W. Wang, B. Lu, D. Gao, Simulation study on the adsorption characteristics of CO2 and CH4 by oxygen-containing functional groups on coal surface, Energy Sources Part A Recovery Util. Environ. Eff. 44 (2022) 3709–3719.
[53] Z. Li, D. Liu, Y. Cai, Y. Wang, J. Teng, Adsorption pore structure and its fractal characteristics of coals by $N_2$ adsorption/desorption and FESEM image analyses, Fuel 257 (2019) 116031.
[54] A. Liu, S. Liu, K. Zhang, K. Xia, Competitive sorption of $CH_4$ and $CO_2$ on coals: implications for carbon geo-storage, Sep. Purif. Technol. 354 (2025) 129399, https://doi.org/10.1016/j.seppur.2024.129399.
[55] Y. Liu, J. Wilcox, Effects of surface heterogeneity on the adsorption of CO2 in microporous carbons, Environ. Sci. Technol. 46 (2012) 1940–1947.
[56] M. Mastalerz, L. He, Y.B. Melnichenko, J.A. Rupp, Porosity of coal and shale: insights from gas adsorption and SANS/USANS techniques, Energy Fuels 26 (2012) 5109–5120.
[57] S. Merey, C. Sinayuc, Analysis of carbon dioxide sequestration in shale gas reservoirs by using experimental adsorption data and adsorption models, J. Nat. Gas. Sci. Eng. 36 (2016) 1087–1105.
[58] M. Mukherjee, S. Misra, A review of experimental research on enhanced coal bed methane (ECBM) recovery via $CO_2$ sequestration, EarthSci. Rev. 179 (2018) 392–410.
[59] Oprisan, M., 2011. Prospects for Coal and Clean Coal Technologies in Kazakhstan, IEA Clean Coal Centre, London, UK.
[60] Reichl, C., Schatz, M., 2024. World Mining Data 2024, Vol. 39. Federal Ministry of Finance, Republic of Austria, Vienna.
[61] R.F. Sachsenhofer, A. Bechtel, D. Reischenbacher, A. Weiss, Evolution of lacustrine systems along the miocene Mur-Mürz fault system (Eastern Alps) and implications on source rocks in pull-apart basins, Mar. Pet. Geol. 20 (2003) 83–110, https://doi.org/10.1016/S0264-8172(03)00018-7.
[62] S. Sadasivam, S. Masum, M. Chen, K. Stanczyk, H. Thomas, Kinetics of gas phase CO2 adsorption on bituminous coal from a shallow coal seam, Energy Fuels 36 (2022) 8360–8370.
[63] R.M. Sadykov, V.V. Korobkin, Geological input data analysis for basin modeling of the south part of karaganda coal deposit: news of The National academy of sciences of the Republic of Kazakhstan, Ser. Geol. Tech. Sci. 1 (433) (2019) 133–142, https://doi.org/10.32014/2019.2518-170X.17.
[64] M. Safaei-Farouji, D. Misch, R.F. Sachsenhofer, A review of influencing factors and study methods of carbon capture and storage (CCS) potential in coals, Int. J. Coal Geol. 277 (2023) 104351, https://doi.org/10.1016/j.coal.2023.104351.
[65] M. Safaei-Farouji, D. Misch, R.F. Sachsenhofer, M. Rauscher, N. Kostoglou, From abandoned mines to carbon sinks: assessing the CO2 storage capacity of Austrian low-rank coal deposits, Int. J. Coal Geol. 286 (2024) 104495, https://doi.org/10.1016/j.coal.2024.104495.
[66] M. Safaei-Farouji, D. Misch, R.F. Sachsenhofer, F. Knabl, N. Kostoglou, Hybrid Chemisorption–Physisorption of subcritical $CO_2$ on coals: implications for safe and Long-Term underground $CO_2$ sequestration, Energy Fuels 39 (25) (2025) 12054–12063.
[67] P. Sang, Y.Q. Chen, M.T. Liu, Y.T. Wang, T. Yue, Y. Li, Y.R. Yin, L.Q. Yang, Electrostatic interactions are the primary determinant of the binding affinity of SARS-CoV-2 spike RBD to ACE2: a computational case study of omicron variants, Int. J. Mol. Sci. 23 (2022) 14796.
[68] Satibekova, S.B., 2019. Creation of a Geological and Geophysical Model for Forecasting the Stability of Roof Rocks of Coal Seams in the Karaganda basin (PhD thesis), Karaganda Technical University, 133.
[69] C. Scherdel, G. Reichenauer, M. Wiener, Relationship between pore volumes and surface areas derived from the evaluation of N2-sorption data by DR-, BET-and t-plot, Microporous Mesoporous Mater. 132 (2010) 572–575.
[70] A.V. Skoblenko, K.E. Degtyarev, A.V. Travin, V.G. Batanova, A.Y. Skuzovatov, N. A. Kanygina, A.A. Tretyakov, A.N. Larinov, K.M. Ryazantsev, Two episodes of early palaeozoic high-pressure metamorphism in north balkhash ophiolite zone (Central Kazakhstan, Western Central Asian Orogenic Belt): evidence for tectonic evolution of Junggar–Balkhash ocean, Lithos 482-483 (2024) 107672, https://doi.org/10.1016/j.lithos.2024.107672.
[71] Y. Song, Q. Zou, E. Su, Y. Zhang, Y. Sun, Changes in the microstructure of low-rank coal after supercritical CO2 and water treatment, Fuel 279 (2020) 118493.
[72] E. Su, Y. Liang, Q. Zou, Structures and fractal characteristics of pores in long-flame coal after cyclical supercritical CO2 treatment, Fuel 286 (2021) 119305.
[73] R. Sykes, L.R. Snowdon, Guidelines for assessing the petroleum potential of coaly source rocks using Rock-Eval pyrolysis, Org. Geochem. 33 (12) (2002) 1441–1455.
[74] Taylor, G., Teichmüller, M., Davis, A., Diessel, C.F.K., Littke, R., Robert, P., 1998. Organic Petrology. Gebrüder Borntraeger, Berlin.
[75] M. Thommes, K. Kaneko, A.V. Neimark, J.P. Olivier, F. Rodriguez-Reinoso, J. Rouquerol, K.S. Sing, Physisorption of gases, with special reference to the evaluation of surface area and pore size distribution (IUPAC Technical Report), Pure Appl. Chem. 87 (2015) 1051–1069.
[76] F. van Bergen, H.J.M. Pagnier, B.M. Krooss, L.G.H. van der Meer, $CO_2$ - sequestration in the Netherlands: inventory of the potential for the combination of subsurface carbon dioxide disposal with enhanced coalbed methane production, in: D. Williams, R. Durie, P. McMullan, C. Paulson, A. Smith (Eds.), Proceedings of the 5th Int. Conf. on Greenhouse Gas Control Technologies, CSIRO Publishing, Collingwood, VIC, Australia, 2001, pp. 555–560.
[77] S. Vranjes-Wessely, D. Misch, I. Issa, D. Kiener, R. Fink, T. Seemann, B. Liu, G. Rantitsch, R.F. Sachsenhofer, Nanoscale pore structure of carboniferous coals from the Ukrainian Donets basin: a combined HRTEM and gas sorption study, Int. J. Coal Geol. 224 (2020) 103484.
[78] J. Wang, Y. Chen, H. Yao, H. Li, C. Wang, Study on directed modification mechanism of surface functional groups of anthracite by supercritical CO2 for improved adsorption, Fuel 386 (2025) 134196.
[79] X. Wang, H. Liu, D. Zhang, X. Yuan, P. Zeng, H. Zhang, Effects of CO2 adsorption on molecular structure characteristics of coal: implications for CO2 geological sequestration, Fuel 321 (2022) 124155.
[80] Z. Weishauptová, J. Medek, L. Kovář, Bond forms of methane in porous system of coal II, Fuel 83 (13) (2004) 1759–1764.
[81] P. Weniger, W. Kalkreuth, A. Busch, B.M. Krooss, High-pressure methane and carbon dioxide sorption on coal and shale samples from the Paraná basin, Brazil, Int. J. Coal Geol. 84 (2010) 190–205.
[82] C.M. White, D.H. Smith, K.L. Jones, A.L. Goodman, S.A. Jikich, R.B. LaCount, S. B. DuBose, E. Ozdemir, B.I. Morsi, K.T. Schroeder, Sequestration of carbon dioxide in coal with enhanced coalbed methane recovery a review, Energy Fuels 19 (2005) 659–724.
[83] P. Zhang, D. Misch, F. Hu, N. Kostoglou, R.F. Sachsenhofer, Z. Liu, Q. Meng, A. Bechtel, Porosity evolution in organic matter-rich shales (Qingshankou Fm.; Songliao Basin, NE China): implications for shale oil retention, Mar. Pet. Geol. 130 (2021) 105139.
[84] J. Zhao, H. Xu, D. Tang, J.P. Mathews, S. Li, S. Tao, A comparative evaluation of coal specific surface area by $CO_2$ and $N_2$ adsorption and its influence on $CH_4$ adsorption capacity at different pore sizes, Fuel 183 (2016) 420–431.
[85] Q. Zou, B. Lin, Fluid–solid coupling characteristics of gas-bearing coal subjected to hydraulic slotting: an experimental investigation, Energy Fuels 32 (2) (2018) 1047–1060.
[86] Q.L. Zou, B.Q. Lin, T. Liu, Y. Zhou, Z. Zhang, F.Z. Yan, Variation of methane adsorption property of coal after the treatment of hydraulic slotting and methane pre-drainage: a case study, J. Nat. Gas Sci. Eng. 20 (2014) 396–406.